Combustion and Flame 249 (2023) 112530

Contents lists available at ScienceDirect

Combustion and Flame

journal homepage: www.elsevier.com/locate/combustflame

Cost-constrained adaptive simulations of transient spray combustion in a gas turbine combustor

Danyal Mohaddes*, Davy Brouzet, Matthias Ihme

Department of Mechanical Engineering, Stanford University, CA 94305, USA

ARTICLE INFO

Article history:
Received 29 April 2022
Revised 19 November 2022
Accepted 21 November 2022

Keywords:
Spray combustion
Combustion modeling
Adaptive modeling
Lean blow-out

ABSTRACT

Predictive high-fidelity simulations of turbulent spray combustion must capture the combined effects of complex chemistry, multiphase evaporating flow and spray-flame interactions to achieve physical accuracy. Finite-rate chemistry (FRC) combined with a realistic chemical mechanism is a combustion model well-suited for this purpose, but has a high computational cost due to the large number and stiffness of transported chemical species. In contrast, flamelet-based models achieve lower cost by transporting a small number of quantities of reduced stiffness, but assumptions regarding local flame topology, boundary conditions and inter-phase coupling limit their physical accuracy. Recently, the Pareto-efficient combustion (PEC) framework was developed to dynamically assign combustion models based on local cost and accuracy metrics in gas-phase reacting flows. In this work, we extend this PEC framework to spray combustion through the rigorous analysis of the multiphase coupling terms in the governing equations. The derivation shows that spray evaporation causes errors in the prediction of species mass fractions for flamelet-based models due to the sensitivity of the local thermo-chemical state to changes in composition caused by fuel vaporization across combustion regimes present in practical spray combustion devices. Sub-model assignment is formulated as a multiple-choice knapsack problem, where computational cost is directly controlled through the fraction of the domain assigned to the FRC sub-model. The extended PEC formulation is applied to the simulation of a realistic rich-quench-lean gas turbine combustor at steady-state conditions, as well as transient operation resulting in lean blow-out (LBO). Analysis of transient simulations during LBO demonstrates the extended PEC formulation's capacity to dynamically adapt to changing conditions within the combustor. Transient combustor dynamics are shown to approach convergence with limited increases in computational cost, while retaining substantial computational cost reduction compared to monolithic FRC simulations. Through PEC simulations with increasing fractions of the domain assigned to FRC, monolithic flamelet simulations are shown to over-predict flame stability during LBO. The extended PEC formulation is thus shown to overcome deficiencies of monolithic models by controlling modeling error for multiphase combustion modeling.

1. Introduction

The combustion of liquid fuel remains an important area of research due to its continued use in automotive, aeronautical and space propulsion applications. Computational simulations of such systems using large-eddy simulation (LES) are a key tool for their design and analysis, offering detailed information and robust control of boundary conditions. LES of chemically reactive flows relies upon combustion models to describe the local chemistry and its effects on the fluid dynamics. Combustion modeling for multiphase turbulent reacting flows presents multiple challenges. Since practical spray combustion systems typically employ heavy hydrocarbon fuels, the accurate representation of the complex chemistry necessitates the consideration of large chemical mechanisms [1]. Practical fueling systems inject polydisperse sprays into highly turbulent flow environments, resulting in spatially heterogeneous droplet evaporation behavior that directly affects the instantaneous distribution and mixing of fuel vapor [2], resulting in a range of complex local flame structures. This is particularly significant in swirl-stabilized systems [3]. Direct spray-flame interaction can occur, with droplets penetrating the flame and continuing to modify the local chemistry outside of the primary reaction zone [4]. The reliability of the results obtained through simulations, particularly for quantities of interest (QoIs) such as emissions concentrations, is directly influenced by the accuracy of the combustion model employed and its ability to capture these complex effects. At the same

* Corresponding author, currently at FM Global Research.
E-mail address: danyal.mohaddes@fmglobal.com (D. Mohaddes).

https://doi.org/10.1016/j.combustflame.2022.112530
0010-2180/

time, the utility of a combustion model for use in simulations also depends upon the associated computational cost – an intractable computational cost would preclude the application of a model to practical configurations. Therefore, substantial effort has been dedicated to the development of spray combustion models.

A variety of approaches have been taken to spray combustion modeling. Here, we briefly summarize those in use in the recent literature. Finite rate chemistry (FRC) is a topology-free spray combustion model involving the solution of transport equations for all species in a given chemical mechanism and requires the computation of the chemical source term for each species [3]. With a sufficiently detailed chemical mechanism for the fuel and oxidizer considered, highly accurate solutions can be obtained across a wide range of combustion regimes [5], minimizing the effects of model assumptions on predictions of QoIs. However, computational cost can be substantial, particularly for large hydrocarbon mechanisms having around 40 to 100 species [6]. Turbulence-chemistry interaction (TCI) can be accounted for using a number of models [7], with the dynamic thickened flame model [8] being among the most commonly employed.

There exists a large class of flamelet-based tabulated chemistry models that are employed for spray combustion modeling. In these models, all species mass fractions and source terms are described by a low-dimensional manifold pre-tabulated from laminar flame simulations [9,10]. In the pre-vaporized flamelet progress-variable approach (FPV) [2,11], counterflow diffusion flame simulations are tabulated across a range of scalar dissipation rates by considering a gaseous fuel stream with a reduced temperature to account for the latent heat of vaporization. The flamelet-generated manifold (FGM) [12] is a similar model, where tabulation is performed by considering unstrained, premixed gaseous flames across a range of fuel-air equivalence ratios. In flamelet-based models, manifold-describing variables are the mixture fraction and the progress variable. Only these two variables are transported in the simulation, with chemical reactivity described solely by the source term of the progress variable. Species mass fractions, the progress variable source term, as well as thermo-chemical and transport properties are retrieved by table look-up using the manifold-describing variables. These models are strictly valid only in adiabatic flows with large group-combustion numbers [13], where the spray has fully vaporized prior to combustion and direct spray-flame interactions do not occur. TCI is commonly considered using the dynamic thickened flame model [14], or by using a presumed probability density function (PDF) closure for filtered quantities and transporting the mixture fraction variance as a third manifold-describing variable [10]. The small number of transported variables results in a substantial reduction in computational cost as compared to FRC, but limits simulation accuracy, as has been shown through direct comparisons of spray combustion simulations employing FRC and FPV [15,16].

An alternative tabulated method to the FPV model is the spray-flamelet progress-variable approach (Spray-FPV) [17]. In this model, counterflow spray flames are tabulated, where the fuel stream consists of a multiphase flow of liquid fuel with oxidizer as a carrier gas. The manifold-describing variables are the same as for FPV, and TCI is commonly accounted for through the transported PDF method [18]. Spray-FPV captures some effects of fuel vaporization on the reacting flow more accurately than FPV and has been applied with success to canonical laminar and turbulent spray flame configurations [19,20]. However, it is strictly valid only for monodisperse sprays in adiabatic flows and requires prescription of fixed values in the fuel stream for the fuel-air ratio, the monodisperse droplet diameter and the droplet velocity [20], giving it limited applicability to practical multi-stage and polydisperse spray combustion systems.

In practical analyses, modeling choices are often constrained by the associated computational costs. The combustion models yielding the highest levels of physical fidelity are commonly also those that have the greatest computational cost, leading to a necessary trade-off between cost and accuracy for any given simulation. Recently [21], it was demonstrated that much of the domain in combustion simulations is in fact well-described by simple flow-physics models of lower cost, such as inert mixing and equilibrium flamelets. This is because the thermo-chemistry in the majority of the computational domain corresponds either to inert or equilibrated flame structures, by virtue of flames generally being spatially compact. It was therefore proposed [21,22] to perform a dynamic optimization of this model assignment problem, where instead of applying a monolithic combustion model to the entirety of the domain, combustion models were selected locally based on considerations of modeling error and computational cost. The local modeling error is estimated using the drift terms of a number of QoIs, where the drift term of a QoI is obtained by comparing its local material derivative when computed using the available combustion models (termed 'sub-models') [21]. QoIs are selected as the mass fractions of major and minor chemical species. An optimization procedure is then used to dynamically assign sub-models throughout the domain. It has been demonstrated [21] that the computational cost and modeling error of a simulation form a Pareto-optimal front, and a user-provided parameter is thus employed to select the desired level of trade-off between cost and error based on the needs of the user. This formulation, referred to as Pareto-efficient combustion (PEC), was developed for gas-phase reacting flows and results in a heterogeneous field of combustion model assignments.

The objective in this work is to extend the PEC formulation to spray combustion. Dynamic model assignment for spray combustion requires an accurate assessment of the local modeling errors, in particular the error arising from modifications to the local thermo-chemistry by spray evaporation. To this end, we perform a rigorous analysis of the governing equations to derive an extended definition of the drift term as an error metric for QoIs in multiphase turbulent reacting flows. To improve upon the model assignment algorithm of previous works [21–23], we consider a constrained optimization procedure [24]. This allows us to minimize modeling errors subject to a user-specified limit of computational cost, instead of prescribing an arbitrary weighting of cost and error to be minimized simultaneously.

We evaluate the extended formulation through its application to a realistic gas turbine combustor that is operated with liquid fuel. The configuration considered, referred to as the FAA Referee Rig [25], is representative of a single-nozzle rich-quench-lean (RQL)-type combustor. Various chemical mechanisms and combustion models have been employed in simulations of the Referee Rig. Esclapez et al. [2] employed FPV, with chemistry tabulated from the 112-species HyChem mechanism [1]. Other groups [26,27] employed FRC, but due to the computational cost associated with transporting scalars throughout the complex practical geometry of the Referee Rig, they considered chemical mechanisms with reduced stiffness and number of species. This is emblematic of the trade-off between computational cost and model accuracy in practical LES noted above. In this work, we apply our extended PEC framework to simulations of the Referee Rig to achieve an optimal trade-off, reducing computational cost in zones of low chemical reactivity and flame structure complexity, and dynamically adapting the combustion model assignment to changes in the flow field during LBO for a constant, user-specified computational cost. We consider simulations of steady-state conditions to allow for comparisons to experimental data and consideration of sub-model assignment statistics; however, we focus our simulation and analysis

efforts on LBO, since this is the more challenging environment for dynamic sub-model assignment.

The main contributions of this work are fourfold: (i) the PEC framework is extended to spray combustion by analyzing the governing equations; (ii) the extended definition of the drift term is used as a standalone metric for estimating modeling error in multiphase reacting flows; (iii) the model assignment problem is reposed as a cost-constrained optimization problem with direct user control instead of using a relative weighting of computational cost and modeling error, and (iv) the aforementioned contributions are employed in simulations of LBO in a gas turbine combustor.

The remainder of this manuscript is organized as follows. The governing equations for the multiphase reacting flow are presented in Section 2. The PEC framework is presented in Section 3, and its extension to spray combustion is derived. The configuration of the Referee Rig is presented in Section 4, and simulation results are discussed in Section 5. The manuscript closes with conclusions in Section 6.

2. Governing equations

We consider the governing equations for a multiphase reacting flow in the context of LES. The Favre-filtered equations for the gaseous phase, with source terms in each equation arising from exchanges with the liquid phase, are [28]

$$D_t\bar{\rho} = -\bar{\rho}\nabla\cdot\tilde{\boldsymbol{u}} + \bar{\dot{S}}_\rho, \tag{1a}$$

$$\bar{\rho}D_t\tilde{\boldsymbol{u}} = -\nabla\bar{p} + \nabla\cdot\overline{\boldsymbol{\tau}}_{\nu+t} + \bar{\dot{\boldsymbol{S}}}_{\rho u}, \tag{1b}$$

$$\bar{\rho}D_t\tilde{e}_t = -\nabla\cdot(\bar{p}\tilde{\boldsymbol{u}}) + \nabla\cdot(\bar{\tau}_{\nu+t}\cdot\tilde{\boldsymbol{u}}) - \nabla\cdot\overline{\boldsymbol{q}}_{\nu+t} + \bar{\dot{S}}_{\rho e_t}, \tag{1c}$$

$$\bar{\rho}D_t\tilde{Y}_\alpha = -\nabla\cdot\bar{\boldsymbol{j}}_{\alpha,\nu+t} + \bar{\dot{\omega}}_\alpha + \bar{\dot{S}}_{\rho Y_\alpha},\ \alpha = 1\ldots N_s-1 \tag{1d}$$

where ρ is the density, $\boldsymbol{u}$ is the velocity vector, p is the pressure, $\boldsymbol{\tau}$ is the stress tensor, e_t is the specific total energy, $\boldsymbol{q}$ is the heat flux, Y_α is the species mass fraction, $\boldsymbol{j}_\alpha$ is the species flux, and $\dot{\omega}_\alpha$ is the species source term. Tildes and overbars denote Favre and Reynolds filtering, respectively. Subscripts ν and t denote molecular and turbulent contributions, respectively, and the subscript α denotes the αth species. Coupling from the liquid phase to the gas phase is achieved through the inter-phase exchange terms $\bar{\dot{S}}_\xi$, where ξ are conservative Eulerian variables. The system is closed with the ideal gas equation of state.

The multiphase flow is considered through a two-way coupled Eulerian–Lagrangian formulation. Each Lagrangian droplet is governed by Miller et al. [29]

$$d_t\boldsymbol{x}_d = \boldsymbol{u}_d, \tag{2a}$$

$$d_t\boldsymbol{u}_d = \tfrac{f_1}{\tau_d}(\tilde{\boldsymbol{u}} - \boldsymbol{u}_d), \tag{2b}$$

$$d_t T_d = \tfrac{\mathrm{Nu}}{3\,\mathrm{Pr}_g}\tfrac{c_p}{c_l}\tfrac{f_2}{\tau_d}\left(\tilde{T} - T_d\right) + \tfrac{L_v}{c_l}\tfrac{\dot{m}_d}{m_d}, \tag{2c}$$

$$d_t m_d \equiv \dot{m}_d = -\tfrac{\mathrm{Sh}}{3\mathrm{Sc}_g}\tfrac{m_d}{\tau_d}H_M, \tag{2d}$$

where $\boldsymbol{x}_d$, $\boldsymbol{u}_d$, T_d, m_d and $\dot{m}_d$ are the droplet position, velocity, temperature, mass and mass evaporation rate, respectively, and $\tau_d \equiv \rho_l d^2/(18\mu)$ is the droplet relaxation time, where ρ_l and d are the droplet density and diameter, respectively, and μ is the gas-phase dynamic viscosity. The gas-phase temperature and velocity $\tilde{T}$ and $\tilde{\boldsymbol{u}}$ are evaluated at the droplet position. Pr_g and Sc_g are the gas-phase Prandtl and Schmidt numbers, respectively, c_p is the gas-phase heat capacity, and L_v and c_l are the heat of vaporization and liquid heat capacity, respectively. The coefficients Nu and Sh are the droplet Nusselt and Sherwood numbers [30], and f_1 is the Stokes drag correction [29]. A non-equilibrium Langmuir–Knudsen model (model M7 in Miller et al. [29]) is used to close the evaporative heat transfer correction f_2 and mass transfer potential H_M. Due to the size and slip velocities of droplets in the present study, a secondary droplet breakup (SBU) model is employed [31]. Droplets having a Weber number $\mathrm{We} = \rho_l u_s^2\, d/\sigma$ greater than a critical value of $\mathrm{We}_c = 7$ undergo a stochastic breakup process, where $u_s = ||\tilde{\boldsymbol{u}} - \boldsymbol{u}_d||$ is the local slip velocity and σ is the surface tension.

The instantaneous projection of the action of the Lagrangian liquid phase to the Eulerian gas phase for any conservative variable ξ at any location $\boldsymbol{x}$ in the computational domain is achieved via the source terms in Eq. (1) defined as in Boivin et al. [32]

$$\bar{\dot{S}}_\xi(\boldsymbol{x}) = \sum_{i=1}^{N_d}\Xi_{d,i}\int_\Omega A(\boldsymbol{x}_{d,i}-\boldsymbol{x}')G(\boldsymbol{x}-\boldsymbol{x}')d\boldsymbol{x}' \equiv \sum_{i=1}^{N_d}\Xi_{d,i}\chi(\boldsymbol{x};\boldsymbol{x}_{d,i}), \tag{3}$$

where for each droplet i of the N_d total droplets present in the domain, $\Xi_{d,i}$ is the extensive point source of ξ, A is the particle source distribution, G is the LES filter, χ is a shorthand notation for the integral and Ω is the computational domain [33]. Taking $A = \delta$, where δ is the Dirac delta function, and $G = \Delta$, where Δ is a top-hat filter for the discretized finite-volume grid, yields the 'particle-in-cell' formulation employed in this study. Sub-grid scale spray dispersion is not considered in this study. In the general case of multi-component droplets undergoing preferential evaporation, taking $\xi = \bar{\rho}\tilde{Y}_f$ yields $\Xi_{d,i} = \dot{m}_{d,i,\alpha}$, where $\dot{m}_{d,i,\alpha}$ is the mass evaporation rate of component α from droplet i, and $\tilde{Y}_f$ is the vector of fuel species. In this study, the multi-component fuel spray is modeled using a single liquid species, and thus taking $\xi = \bar{\rho}\tilde{Y}_f$ yields $\Xi_{d,i} = \dot{m}_{d,i}\delta_{\alpha,f}$, where $\dot{m}_{d,i}$ is the mass evaporation rate of droplet i from Eq. (2), $\delta_{\alpha,f}$ is the Kronecker delta equal to unity only when α is the fuel species, and $\tilde{Y}_f$ is a scalar quantity.

3. Spray-augmented PEC framework

3.1. Derivation of spray combustion drift term

We present the extension of the PEC framework [21] to spray combustion. PEC performs dynamic combustion sub-model assignment based on estimates of local modeling error and computational cost. The local modeling error associated with a given choice of combustion sub-model is not available directly, since this would necessitate evolving each sub-model throughout the entire domain, eliminating any advantage to be gained from dynamic model selection in terms of computational cost. Instead, the local modeling error associated with a QoI ψ for a sub-model m is estimated by introducing the drift term $\mathcal{D}_\psi^m$ [21,34].

The drift term has been described elsewhere in detail as a measure of the growth rate of the departure between combustion model manifolds in LES of gas-phase combustion [22,35]. We summarize that description here, specifically considering the drift term as a first-order estimate of the rate of departure of the predicted value of a QoI ψ when computed using a sub-model m compared to a high-fidelity reference sub-model. We show this idea schematically in Fig. 1, where we consider the temporal evolution of a QoI ψ. Since QoIs are transported quantities, the forward Taylor expansions employ the material derivative, as follows:

$$\tilde{\psi}(t_{n+1}) = \tilde{\psi}(t_n) + \tilde{D}_t(\tilde{\psi}(t_n))\Delta t + \mathcal{O}(\Delta t^2), \tag{4a}$$

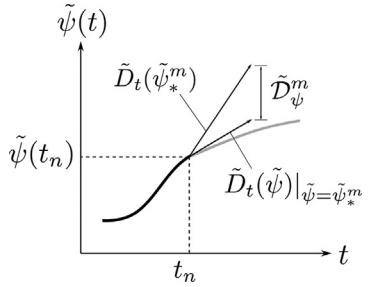

Fig. 1. Schematic illustration of the drift term $\tilde{\mathcal{D}}^m_\psi$ for a QoI ψ and combustion sub-model m. Per Eq. (5), $\tilde{\mathcal{D}}^m_\psi$ is defined using the difference in the advective rates of change of ψ predicted by the high-fidelity reference model and the sub-model m at the instant t_n, $\tilde{D}_t(\tilde{\psi})|_{\tilde{\psi}=\tilde{\psi}^m_*}$ and $\tilde{D}_t(\tilde{\psi}^m_*)$, respectively.

$$\tilde{\psi}^m(t_{n+1}) = \tilde{\psi}^m(t_n) + \tilde{D}_t(\tilde{\psi}^m(t_n))\Delta t + \mathcal{O}(\Delta t^2), \tag{4b}$$

where $t_{n+1} = t_n + \Delta t$. To allow comparison of sub-model predictions and thereby quantification of the rate of departure of the predicted value of ψ, a consistent initial condition at t_n must be employed. We therefore set $\tilde{\psi}(t_n) = \tilde{\psi}^m_*(t_n)$, where the asterisk denotes evaluation of the QoI from the manifold Γ of the sub-model m having a vector of manifold-describing variables $\tilde{\boldsymbol{\phi}}^m$, i.e., $\tilde{\psi}^m_* = \Gamma^m(\tilde{\boldsymbol{\phi}}^m)$. Subtracting Eq. (4b) from Eq. (4a) and rearranging, we find that $\tilde{D}_t(\tilde{\psi})|_{\tilde{\psi}=\tilde{\psi}^m_*} - \tilde{D}_t(\tilde{\psi}^m_*) = \Delta\tilde{\psi}/\Delta t$ to first order, where $\Delta\tilde{\psi} = \tilde{\psi} - \tilde{\psi}^m$ is the difference along the streamline in the predicted value of ψ obtained from the sub-model m after a time Δt compared to that obtained from the high-fidelity reference sub-model. In conservation form, the filtered drift term for a QoI ψ determined from the sub-model m is then defined as Wu et al. [22]

$$\tilde{\mathcal{D}}^m_\psi = \bar{\rho}\tilde{D}_t(\tilde{\psi})|_{\tilde{\psi}=\tilde{\psi}^m_*} - \bar{\rho}\tilde{D}_t(\tilde{\psi}^m_*). \tag{5}$$

We now present a logical extension of the drift term formulation to spray combustion through an analysis of the filtered gaseous equations for a multiphase reacting flow, Eq. (1). Assuming the QoIs are the filtered mass fractions of chemical species, from Eq. (1) the material derivative of $\tilde{\psi}$ can be expressed as a sum of filtered diffusive, reactive and spray terms

$$\bar{\rho}\tilde{D}_t(\tilde{\psi}) = -\nabla\cdot\bar{j}_{\psi,\nu+t} + \bar{\dot{\omega}}_\psi + \bar{\dot{S}}_{\rho\psi} \tag{6}$$

where the spray term $\bar{\dot{S}}$ arises as a result of liquid-to-gas phase coupling. For convenience, we will also define a material derivative that does not take the spray term into account,

$$\bar{\rho}\tilde{D}_{t,0}(\tilde{\psi}) = -\nabla\cdot\bar{j}_{\psi,\nu+t} + \bar{\dot{\omega}}_\psi, \tag{7}$$

and the related drift term

$$\tilde{\mathcal{D}}^m_{\psi,0} = \bar{\rho}\tilde{D}_{t,0}(\tilde{\psi})|_{\tilde{\psi}=\tilde{\psi}^m_*} - \bar{\rho}\tilde{D}_{t,0}(\tilde{\psi}^m_*). \tag{8}$$

In the case of tabulated models, where $\tilde{\psi}^m_* = \Gamma^m(\tilde{\boldsymbol{\phi}}^m)$, the contribution to the drift term is [22]

$$\bar{\rho}\tilde{D}_t(\tilde{\psi}^m_*) = \bar{\rho}\frac{\partial\tilde{\psi}^m_*}{\partial\tilde{\boldsymbol{\phi}}^m}\tilde{D}_t(\tilde{\boldsymbol{\phi}}^m). \tag{9}$$

The drift term can thus be re-expressed as

$$\tilde{\mathcal{D}}^m_\psi = \tilde{\mathcal{D}}^m_{\psi,0} + \left(\bar{\dot{S}}_{\rho\psi}|_{\tilde{\psi}=\tilde{\psi}^m_*} - \frac{\partial\tilde{\psi}^m_*}{\partial\tilde{\boldsymbol{\phi}}^m}\bar{\dot{\boldsymbol{S}}}_{\rho\boldsymbol{\phi}}\right), \tag{10}$$

which gives rise to the definition

$$\tilde{\mathcal{D}}^m_{\psi,d} = \bar{\dot{S}}_{\rho\psi}|_{\tilde{\psi}=\tilde{\psi}^m_*} - \frac{\partial\tilde{\psi}^m_*}{\partial\tilde{\boldsymbol{\phi}}^m}\bar{\dot{\boldsymbol{S}}}_{\rho\boldsymbol{\phi}} \tag{11}$$

and hence

$$\tilde{\mathcal{D}}^m_\psi = \tilde{\mathcal{D}}^m_{\psi,0} + \tilde{\mathcal{D}}^m_{\psi,d}, \tag{12}$$

where $\tilde{\mathcal{D}}^m_{\psi,d}$ is the contribution to the drift term arising from the spray source terms and $\bar{\dot{\boldsymbol{S}}}_{\rho\boldsymbol{\phi}}$ is the vector of filtered source terms of $\tilde{\boldsymbol{\phi}}^m$ arising from the spray phase.

A strength of the PEC framework is that QoIs are user-specified, whereby users can select a vector of arbitrary length of quantities that are relevant to determining the intended accuracy metrics of their simulation. In spray combustion applications, it is common that fuel species rapidly pyrolyze after vaporization [1], making the fuel species themselves unlikely candidates for QoIs. More appropriate QoIs are emissions and products of incomplete combustion, such as CO and H_2, and major species indicative of heat release, such as CO_2 and H_2O. The first term in $\tilde{\mathcal{D}}^m_{\psi,d}$ is non-zero if and only if $\tilde{\psi} \in \tilde{Y}_f$, where $\tilde{Y}_f$ is the vector of species constituting the potentially multi-component liquid fuel. Setting this term to zero, the general form of Eq. (11) simplifies to

$$\tilde{\mathcal{D}}^m_{\psi,d} = -\frac{\partial\tilde{\psi}^m_*}{\partial\tilde{\boldsymbol{\phi}}^m}\bar{\dot{\boldsymbol{S}}}_{\rho\boldsymbol{\phi}}. \tag{13}$$

The Jacobian on the right-hand-side is evaluated from the tabulated manifold. The filtered source term of $\tilde{\boldsymbol{\phi}}^m$ arising from the spray, $\bar{\dot{\boldsymbol{S}}}_{\rho\boldsymbol{\phi}}$, is not known directly, and must be obtained via partial differentiation from the fuel vapor source term $\bar{\dot{S}}_{\rho Y_f}$ as

$$\bar{\dot{\boldsymbol{S}}}_{\rho\boldsymbol{\phi}} = \frac{\partial\tilde{\boldsymbol{\phi}}^m}{\partial\tilde{Y}_f}\bar{\dot{S}}_{\rho Y_f}. \tag{14}$$

In the case of a multi-component fuel, $\tilde{Y}_f$ and $\bar{\dot{S}}_{\rho Y_f}$ are vector quantities, where the computation of $\bar{\dot{S}}_{\rho Y_f}$ was discussed in Section 2. The need for partial differentiation in Eq. (14) is a consequence of the independence of spray evaporation models and combustion models: the former can only provide direct information regarding the fuel species, not the manifold-describing variables of the latter.

3.2. Combustion sub-models

In this study we consider three combustion sub-models, namely inert mixing (IM), FPV and FRC. The FPV and FRC sub-models are chosen because they represent two extremes in terms of cost and accuracy for spray combustion modeling, as discussed in Section 1. FRC is a more computationally intensive and accurate sub-model than FPV when a realistic chemical mechanism is employed, as is the case in this study. In particular, since FRC makes no assumptions regarding flame topology, it naturally incorporates the effects of spray evaporation on the reacting flow. In the form employed here, FPV assumes global adiabaticity and a local diffusion flame structure, and is therefore ill-suited to spray combustion outside of a pre-vaporized context. FPV is chosen over Spray-FPV, since as discussed in Section 1, the latter requires prescription of quantities such as a monodisperse droplet diameter and a fuel-air ratio for manifold generation. These quantities are highly spatio-temporally heterogeneous in the practical combustor geometry considered in this study, particularly during the transient phenomenon of LBO.

The manifold-describing variables for the FRC sub-model are all the species mass fractions in the chemical mechanism, and mass fractions are obtained by solving Eq. (1d). It is therefore employed as the high-fidelity reference sub-model in this study. The FRC manifold mapping function Γ thus produces an identity mapping, resulting in a drift of $\tilde{\mathcal{D}}^{\mathrm{FRC}}_\psi = 0$ for all QoIs [22]. For the FPV model, the manifold-describing variables are $\tilde{\boldsymbol{\phi}}^{\mathrm{FPV}} = [\tilde{Z}, \tilde{C}]$, where $\tilde{Z}$ and $\tilde{C}$

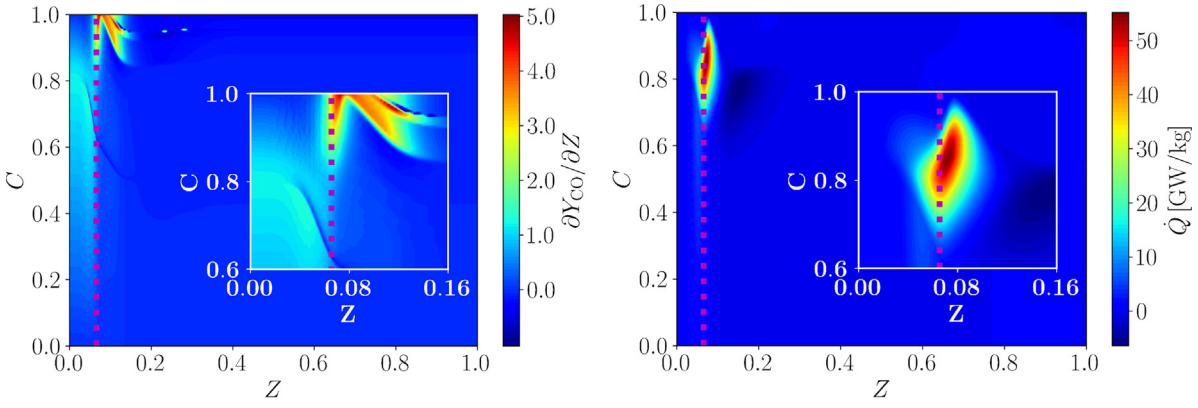

(a) Y_{CO} sensitivity (b) Heat release rate

Fig. 2. Pre-computed results for the FPV sub-model as a function of Z and C, with the stoichiometric mixture fraction $Z_{st} = 0.064$ indicated by the dotted magenta line. The inset figures provide further detail in the region of highest heat release rate. (a) Chemical sensitivity of spray drift term for QoI $\psi = Y_{CO}$, and (b) heat release rate.

are the filtered mixture fraction and the filtered progress variable, with the progress variable defined as the sum of the CO, CO_2, H_2 and H_2O mass fractions [36]. Instead of Eq. (1d), transport equations are solved for $\tilde{Z}$ and $\tilde{C}$ as follows [37]:

$$\bar{\rho} D_t \tilde{Z} = -\nabla \cdot \bar{\jmath}_{Z,v+t} + \bar{\dot{S}}_{\rho Z}, \tag{15a}$$

$$\bar{\rho} D_t \tilde{C} = -\nabla \cdot \bar{\jmath}_{C,v+t} + \bar{\dot{\omega}}_C, \tag{15b}$$

where $\bar{\dot{\omega}}_C$ is obtained from table look-up, as described in Section 1.

The IM sub-model is also considered, which uses a single manifold-describing variable $\tilde{\boldsymbol{\phi}}^{\mathrm{IM}} = [\tilde{Z}]$. Eq. (15a) is solved and Eq. (15b) is considered frozen. This model captures regions where $\bar{\dot{\omega}}_C = 0$, which corresponds primarily to regions of pure reactants where the chemical source term integration is trivial.

The computation of $\tilde{\mathcal{D}}^{\mathrm{FPV}}_{\psi,0}$ and $\tilde{\mathcal{D}}^{\mathrm{IM}}_{\psi,0}$ have been discussed in Wu et al. [21], 22]. We note that outside of regions of pure reactants, $|\tilde{\mathcal{D}}^{\mathrm{IM}}_{\psi,0}| \gg |\tilde{\mathcal{D}}^{\mathrm{FPV}}_{\psi,0}|$. From Eqs. (13), (14), computation of $\tilde{\mathcal{D}}^{\mathrm{FPV}}_{\psi,d}$ requires $\frac{\partial \tilde{\boldsymbol{\phi}}^{\mathrm{FPV}}}{\partial \tilde{Y}_f}$. Assuming $\tilde{Y}_f$ does not contain any of the species constituting the progress variable nor the QoIs, we have $\frac{\partial \tilde{C}}{\partial \tilde{Y}_f} = 0$, and for a single-component fuel, we have $\frac{\partial \tilde{Z}}{\partial \tilde{Y}_f} \approx 1$. After substituting from Eqs. (3), (13) simplifies for FPV to

$$\tilde{\mathcal{D}}^{\mathrm{FPV}}_{\psi,d} = -\frac{\partial \tilde{\psi}^{\mathrm{FPV}}_*}{\partial \tilde{Z}} \sum_{i=1}^{N_d} \dot{m}_{d,i} \chi(\boldsymbol{x}; \boldsymbol{x}_{d,i}), \tag{16}$$

and $\tilde{\mathcal{D}}^{\mathrm{IM}}_{\psi,d}$ follows analogously. This equation makes clear that the contribution of the spray to the drift term is directly proportional to the rate of fuel vapor deposition in the gas phase $\sum_{i=1}^{N_d} \dot{m}_{d,i} \chi(\boldsymbol{x}; \boldsymbol{x}_{d,i})$, which is scaled by the local chemical sensitivity $\frac{\partial \tilde{\psi}^{\mathrm{FPV}}_*}{\partial \tilde{Z}}$. This sensitivity can be considered directly in (Z, C) space for the FPV sub-model. Figure 2 plots the chemical sensitivity for QoI $\psi = Y_{CO}$, as well as the chemical heat release rate $\dot{Q}$, using the chemical mechanism employed for simulations in this study [1,38]. From this figure, it is clear that the largest chemical sensitivity magnitudes are present near the areas of greatest heat release rate around $Z = Z_{st}$, $C \approx 0.9$, shown in the inset figures, as well as fuel-lean compositions with $0.4 < C < 0.9$. In much of the rest of the domain, the sensitivity is near zero, including along the Z, $C = 0$ mixing line relevant to the IM sub-model. This indicates the power of the present formulation: the spray contribution to drift terms will be greatest when direct spray-flame interaction occurs (where chemical sensitivity is high), but only inasmuch as the spray-flame interaction results in spray evaporation – the mere presence of spray is not sufficient to generate additional modeling errors. Thus, $\tilde{\mathcal{D}}^{\mathrm{FPV}}_{\psi,d}$ captures the drift caused by the interphase coupling, where the spray-phase physics cause the gas-phase chemistry to drift from the FRC manifold. Furthermore, $\tilde{\mathcal{D}}^{\mathrm{IM}}_{\psi,d} = 0$ due to negligible chemical sensitivity along the mixing line. This yields the expected result that inert spray evaporation does not generate modeling error for the IM sub-model. IM modeling error is due entirely to its lack of chemistry: $|\tilde{\mathcal{D}}^{\mathrm{IM}}_{\psi}| = |\tilde{\mathcal{D}}^{\mathrm{IM}}_{\psi,0}| \gg |\tilde{\mathcal{D}}^{\mathrm{FPV}}_{\psi}|$ where $\bar{\dot{\omega}}_C \neq 0$. To provide a clear representation of the behavior of the drift terms arising from both gaseous and liquid phase effects, a one-dimensional spray flame is analyzed in the Appendix A. To this end, a wall-stagnating configuration is considered, with boundary conditions chosen to be both representative of the conditions in the combustor and to result in direct spray-flame interaction. The results show that the greatest drift occurs in regions of high chemical sensitivity, direct spray-flame interaction and non-adiabaticity, with drift terms approaching zero in chemically inert regions.

To ensure consistent representations of transport processes throughout the domain, the computation of the molecular and turbulent diffusive quantities in Eq. (1) is performed following the work of Wu et al. [22]. In FRC, species-specific molecular diffusivities are employed, whereas FPV employs a unity molecular Lewis number. Differences in diffusivity arising from the sub-models is accounted for in the gas-phase portion of the drift term per Eqs. (8) and (9); the contribution of diffusion to gas-phase drift is small compared to that of chemical reactivity in the present configuration. Since the unity-Lewis mixture fraction cannot be reconstructed from the FRC transported species, the unity-Lewis mixture fraction is transported in IM and FPV regions, where it is a part of the model formulation, as well as in FRC regions, where its local cost is negligible, but thereby allows a consistent representation throughout the domain [22]. Turbulent species and thermal diffusivities employ identical closures in all models, namely constant turbulent Schmidt and Prandtl numbers of 0.4 and 0.9, respectively, in non-thickened regions, and the thickened flame approach in regions where flame thickening is active.

We note finally that the computation of $\dot{m}_d$ in Eq. (2) requires the gas-phase chemical composition and temperature. In the present study, where droplets are primarily evaporating in hot

products, the effect of the local combustion model on $\dot{m}_d$ is minor. This is due to the solution of an energy equation in Eq. (1) resulting in a consistent temperature field across sub-models. Furthermore, since the droplets considered consist entirely of fuel species, the vapor properties are well-represented through mixture fraction tabulation.

3.3. Sub-model assignment

We now present the details of how sub-model assignment is achieved. The PEC framework [21] assigns a combustion sub-model m to each location $\boldsymbol{x}$ in the computational domain Ω at a time instant t, represented by the mapping $\mathcal{M}:\Omega\rightarrow M$, where $M=\{m_1,\ldots,m_{N_m}\}$ is the vector of N_m possible sub-models. The assignments are made on the basis of instantaneous local estimates of modeling error e^m and computational cost c^m for each sub-model $m\in M$ through an optimization procedure. As in Wu et al. [22], the computational cost c^m is estimated as a sub-model-specific constant corresponding to the number of transported scalars in the sub-model. For the sub-models considered in the present study (IM, FPV and FRC) this corresponds to the number of manifold-describing variables in each sub-model, i.e., $c^m=|\boldsymbol{\phi}^m|$. The local modeling error e^m is taken as the weighted sum of errors for a set Q of N_Q QoIs, i.e., $Q=\{\psi_1,\ldots,\psi_{N_Q}\}$. Error for each QoI is evaluated using the QoI-specific drift term $\tilde{\mathcal{D}}^m_\psi$ as [22]

$$e^m=\sum_{\psi\in Q}\left|\frac{\tilde{\mathcal{D}}^m_\psi}{B_\psi}\right|, \tag{17}$$

where B_ψ is a QoI-specific normalization constant. In this study, the QoIs are chemical species, and the normalization constant for each species is thus taken as the maximum net mass production rate of species ψ in a stoichiometric premixed gaseous flame at nominal system pressure p_0 and unburned gas temperature T_0 corresponding to the spray combustion system considered.

Previous studies employing PEC [22] formulated the instantaneous model assignment as a global optimization problem, where a Lagrange multiplier λ was used as the user-specified parameter for traversing the Pareto front, as discussed in Section 1. The parameter λ controlled the balance between total computational cost $\mathcal{C}$ and total modeling error $\mathcal{E}$ for a given mapping $\mathcal{M}$. These are defined as

$$\mathcal{C}=\sum_{i=1}^{N_e}\sum_{j=1}^{N_m}c_i^{m_j}\zeta_i^{m_j}, \tag{18a}$$

$$\mathcal{E}=\sum_{i=1}^{N_e}\sum_{j=1}^{N_m}e_i^{m_j}\zeta_i^{m_j}, \tag{18b}$$

where $N_e=|\Omega|$ is the number of control volumes to which combustion sub-models are to be assigned, and $\zeta_i^{m_j}\in\{0,1\}$ is a Boolean value equal to unity when the mapping $\mathcal{M}$ assigns sub-model m_j to control volume i, and zero otherwise. The optimization problem was formulated as

$$\min_{\mathcal{M}:\Omega\rightarrow M}\quad \mathcal{E}+\lambda\mathcal{C}. \tag{19}$$

This formulation had two key drawbacks. The first was that the effect of the Lagrange multiplier on simulation cost could not be known a-priori, necessitating a number of trial simulations of any problem configuration of interest to gauge the effect of λ on the portion of the domain assigned to FRC prior to the production run. The second was that simulation cost could not be enforced to be constant for a given choice of λ, since $\mathcal{E}$ varies in time due to unsteadiness in the local thermochemistry throughout the domain. This is particularly consequential in simulations of globally-transient phenomena.

Recently [24], sub-model assignment was proposed as a constrained optimization problem to maintain constant user-specified computational cost $\mathcal{C}_0$. This approach is an instance of a multiple-choice knapsack problem (MCKP) [39], and is formulated as follows:

$$\begin{aligned}&\min_{\mathcal{M}:\Omega\rightarrow M}\quad &&\mathcal{E}\\ &\text{s.t.}\quad &&\mathcal{C}\leq\mathcal{C}_0.\end{aligned} \tag{20}$$

It is inconvenient, however, to employ Eq. (20) directly, because $\mathcal{C}$ is a non-normalized quantity: it depends on N_e, as well as the cost of each sub-model considered. Since the user must supply a value for C_0, this necessitates a level of computational analysis or trial simulations, which is one of the reasons the Lagrange multiplier formulation was replaced with the MCKP formulation in the first instance. However, unlike the Lagrange multiplier formulation, the MCKP formulation is easily recast to a more convenient form. The minimum and maximum bounds on computational cost correspond to monolithic assignments to the sub-models of the lowest and highest cost, respectively, as follows:

$$\mathcal{C}_{\min}=\sum_{i=1}^{N_e}\min_j c_i^{m_j}, \tag{21a}$$

$$\mathcal{C}_{\max}=\sum_{i=1}^{N_e}\max_j c_i^{m_j}. \tag{21b}$$

We can therefore define a normalized cost κ as

$$\kappa=\frac{\mathcal{C}-\mathcal{C}_{\min}}{\mathcal{C}_{\max}-\mathcal{C}_{\min}}. \tag{22}$$

We then recast Eq. (20) as

$$\begin{aligned}&\min_{\mathcal{M}:\Omega\rightarrow M}\quad &&\mathcal{E}\\ &\text{s.t.}\quad &&\kappa\leq\kappa_0,\\ &&&\kappa\in[0,1],\ \ \kappa_0\in[0,1].\end{aligned} \tag{23}$$

In this formulation, the user need only supply the normalized quantity κ_0. For the special case where $N_m=2$, κ_0 corresponds to the fraction of the domain to be assigned to the model of highest fidelity. In the general case where $N_m>2$, κ_0 is the maximum fraction of the domain that can be assigned the model of highest fidelity. In the latter case, the optimization can result in cost-equivalent assignments employing less of the highest fidelity model and more of the middling models if this results in a lower total error $\mathcal{E}$. The choice of κ_0 allows the user to traverse the cost-error Pareto front, similarly to λ in the Lagrange-multiplier formulation. However, Eq. (23) fully abstracts the formulation from any particular configuration and precludes the need for lengthy computational analyses prior to simulation on the part of the user, and is therefore a more convenient and powerful formulation than that of Eq. (19). The assignment problem of Eq. (23) is the approach employed in the present study. It is solved using the computationally efficient algorithm due to Pisinger [39], which first solves a linearized problem and then performs a small number of iterations to find the optimal solution.

As discussed in Section 3.2, the present study considers the IM, FPV and FRC sub-models. Because IM corresponds to the mixing solution, IM is always assigned in locations where $\tilde{\dot{\omega}}_C=0$, since $e^{\mathrm{IM}}=e^{\mathrm{FPV}}=e^{\mathrm{FRC}}\approx 0$ with $c^{\mathrm{IM}}<c^{\mathrm{FPV}}<c^{\mathrm{FRC}}$. Similarly, where $\tilde{\dot{\omega}}_C\neq 0$, IM is seldom assigned, because $e^{\mathrm{IM}}\gg e^{\mathrm{FPV}}>e^{\mathrm{FRC}}$ while c^{IM} is only moderately lower than c^{FPV}. Therefore, for the choice of sub-models employed in this study, we find that although $N_m=3>2$, κ_0 corresponds closely to the fraction of the domain assigned to the model of highest fidelity, namely FRC.

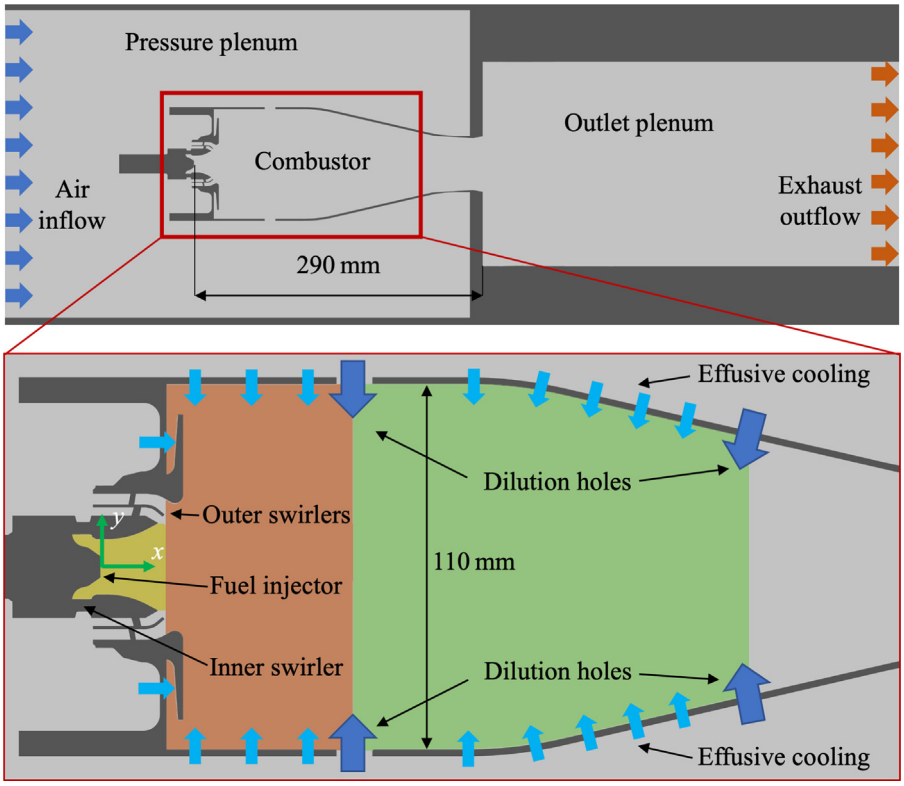

Fig. 3. Schematic of the FAA Referee Rig combustor on the $x-y$ plane. Dark blue, light blue and orange arrows represent primary air flows, effusive air flows and exhaust flow, respectively. Yellow, orange and green background colors indicate the injector region, primary combustion zone and secondary combustion zone, respectively. (For interpretation of the references to color in this figure legend, the reader is referred to the web version of this article.)

4. Experimental and computational configuration

4.1. Experimental setup

As discussed in Section 1, the experimental setup considered is that of a realistic RQL gas turbine combustor that has previously been studied both experimentally [40–42] and numerically [2,43–45]. As part of a collaborative effort under the National Jet Fuels Combustion Program (NJFCP), several academic and industry research groups studied the effects of alternative jet fuels in this configuration. A schematic of this combustor is shown in Fig. 3. The domain consists of four segments: pressure plenum, fuel injector, combustion chamber and outlet plenum. The combustion chamber is further sub-divided into three regions: the injector region, primary combustion zone and secondary combustion zone.

For steady-state conditions, the combustor is operated at the nominal operating point set by the NJFCP, which is a stable condition near LBO. Air enters the primary combustion zone through axial and radial swirlers, and the secondary zone through dilution jets and effusive liners. Liquid Cat-A2 fuel, also referred to as POSF10325 [2,43], is supplied by a pressure-swirl atomizer at a mass flow rate of 2.56 g/s and a temperature of 322 K, yielding a polydisperse spray and a global equivalence ratio of $\phi_g = 0.096$. For blow-out conditions, the fuel flow rate is reduced to 2.06 g/s, resulting in $\phi_g = 0.077$, which is a condition shown experimentally to result in LBO [25]. The chamber is maintained at a pressure of $p_0 = 2.07$ atm, and is supplied with 391.4 g/s of air at a temperature of $T_0 = 394$ K. Flame stabilization is achieved due to a large inner recirculation zone in the primary combustion zone.

The primary and secondary zones of the combustor have a constant height of 110 mm, downstream of which the height is reduced progressively until the exhaust, located 315 mm from the combustor inlet plane. There are two rows of dilution holes located in the upper and lower walls of the combustor. The first row divides the primary and secondary combustion zones, consisting of three holes on each side 70 mm downstream of the fuel injector. The second row consists of four dilution holes on each side 132 mm downstream of the fuel injector. The center of the fuel injector is defined in this study as the origin of the coordinate system. In addition to the swirlers and dilution holes, the pressure plenum supplies air to the combustor through perforations in the upper and lower combustor walls. In the simulations, these are modeled as homogeneous flows through effusive boundaries. Further details of the setup and operating conditions are available in Refs. [2,40,41].

4.2. Combustion chemistry

The fuel considered in this study is liquid Cat-A2 (POSF10325), a conventional petroleum-derived Jet-A fuel. A hybrid approach is taken to modeling the combustion chemistry, referred to as HyChem [1,38]. The multicomponent liquid fuel is represented as a single chemical species having experimentally determined [2,43] thermo-physical properties. The thermal decomposition and oxidative pyrolysis of the fuel vapor are modeled using experimentally constrained, lumped reaction steps [1]. The pyrolysis and oxidation of the products of fuel decomposition are then modeled using reaction chemistry based on the USC Mech II [46], ultimately resulting in the 41-species reduced mechanism with ten quasi-steady-state (QSS) species for the combustion of Cat-A2 in air developed by Wang et al. [1] and Xu et al. [38]. All combustion submodels in this study employ the same chemical mechanism; however, the QSS approximation was not invoked during tabulation for the FPV sub-model and all species were solved directly.

4.3. Numerical methods and computational setup

We employ an unstructured, fully compressible finite-volume solver to solve the governing equations for both gas and liquid phases [47,48]. Convective fluxes are computed using a sensor-based hybrid spatial discretization scheme. Temporal integration is performed using the computationally efficient second-order *Simpler* operator-splitting algorithm for stiff chemistry [49], augmented for multiphase flow by consistently incorporating Lagrangian spray particle updates and inter-phase exchanges of conserved variables. This temporal scheme employs a semi-implicit ODE integrator for the stiff reaction sub-step [49]. The PEC framework's dynamic combustion sub-model assignment algorithm [39] is implemented directly within the solver. The computational mesh employed is the same as employed in previous studies [2,44], and consists of 18.3 million hexahedral elements. A detailed mesh sensitivity study was performed by Hasti et al. [50], and a thorough discussion of the boundary conditions is available in Ref. [2]. Although the PEC formulation is compatible with dynamic load balancing, as has been discussed in previous works [22], the present problem configuration and associated mesh decomposition were found to result in dynamic load balancing having a small impact on computational cost, and it was therefore omitted. Subgrid-scale turbulence is modeled using the Vreman model [51], and TCI is considered using the dynamic thickened-flame model [8] for all sub-models to ensure consistency when comparing quantities between the sub-models [22,23], where in this study we employ a maximum thickening factor of 5. Subgrid-scale flame wrinkling is also considered using the model of Charlette et al. [52], with a maximum efficiency factor of 4.

5. Results

We present the results from an a-priori study as well as a total of six numerical simulations, with two at a steady operating condition and four to analyze transient blow-out dynamics. These simulations are performed for different values of the user-specified cost parameter κ_0, discussed in Section 3.3, in order to evaluate its effect on combustion behavior: $\kappa_0 = 0.0$, $\kappa_0 = 0.01$, $\kappa_0 = 0.06$ and $\kappa_0 = 0.11$. We refer to these model configurations as PEC0, PEC1, PEC6 and PEC11, respectively. The PEC0 model configuration corresponds to a monolithic FPV simulation. Much of the computational domain, shown in Fig. 3, lies outside of the combustor. In the pressure plenum, the chemistry is inert and $e^{\mathrm{IM}} \approx 0$, and in the outlet plenum chemistry is largely equilibrated and $e^{\mathrm{FPV}} \approx 0$. The PEC framework therefore never assigns FRC in these regions, and as discussed in Section 3.3, the values of κ_0 thus correspond closely to the fraction of control volumes assigned to FRC within the combustor. The model configurations considered in this study were chosen initially based on an estimation from the results of previous numerical studies of the flame brush occupying around 5% of the control volumes in the combustor at any instant. We therefore sought to capture the sensitivity of LBO behavior to cost constraints κ_0 selected both below and above this value. The effect of κ_0 on sub-model assignment and combustion dynamics are discussed throughout the following sections.

As discussed in Section 3, the choice of QoIs provide modeling error information to the PEC framework's optimization algorithm through the drift terms, thereby affecting sub-model assignments and ultimately model performance. It is therefore important to select QoIs that are closely related to chemical progress, heat release, locally fuel-rich combustion and emissions. Since the progress variable definition we employ for the FPV sub-model is similarly motivated [36], as was the case in following previous studies employing PEC [21,22], the set Q of QoIs ψ are chosen as the mass fractions of species constituting the progress variable: $Q = \{Y_{\mathrm{CO}}, Y_{\mathrm{CO_2}}, Y_{\mathrm{H_2}}, Y_{\mathrm{H_2O}}\}$. The major products CO_2 and H_2O are closely related to heat release, the minor species CO and H_2 are formed by locally fuel-rich and incomplete combustion, and CO is an important emission for practical analyses.

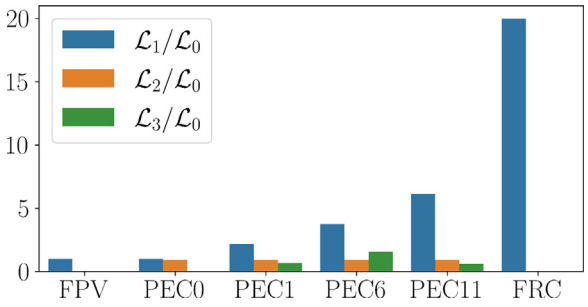

Fig. 4. Average normalized computational performance of model configurations employed in this study. Monolithic FRC is included for comparison, but is not considered for the analysis of physical quantities.

Since the primary aim of employing the PEC model is to reduce the computational cost while achieving high physical fidelity through judicious assignment of combustion sub-models, in Fig. 4 we summarize the average computational performance of the various model configurations considered in this study. All simulations were performed on the same computational architecture to allow performance comparisons. Simulations were performed on a Cray XC40 machine on 64 Intel Haswell nodes with 32 processors per node. The metric used for computational performance is $\mathcal{L}$, the average number of CPU-hours required per millisecond of simulation run time. For ease of comparison, the computational performance metrics reported in Fig. 4 are normalized by that of a monolithic FPV simulation, $\mathcal{L}_0 = 3800$ CPU-hrs/ms. We break down the performance metric $\mathcal{L}$ based on the major operations required in the PEC framework: $\mathcal{L}_1$ is the cost of the advancement of the governing equations Eqs. (1) and (2), $\mathcal{L}_2$ is the cost of drift term evaluation from Eq. (5), $\mathcal{L}_3$ is the cost of solving the sub-model assignment from Eq. (23), and $\mathcal{L} = \sum_{i=1}^{3} \mathcal{L}_i$. In the present configuration, we estimate the normalized performance metric for a monolithic FRC simulation as 20 by analyzing computational performance over approximately 0.1 ms of simulated time, but results for physical quantities are not presented for this model configuration due to the excessively high computational cost. The PEC0 model configuration considered includes drift term and error metric computation to allow analysis of these quantities, and the overhead associated with these computations results in a normalized performance metric of $\mathcal{L}/\mathcal{L}_0 = 1.92$; in the ensuing analysis we therefore consider the PEC0 model configuration instead of monolithic FPV. We find that, by construction, computational cost increases with κ_0 which as noted above corresponds closely to the percentage of the domain assigned to FRC, with the lowest and highest costs being the monolithic FPV and FRC model configurations, respectively. $\mathcal{L}_1$ thus increases with increasing κ_0 due to the FRC sub-model's large number of transported scalars and the stiffness of the associated chemical source terms. $\mathcal{L}_2$ is nearly constant across PEC model configurations, since drift terms are computed for all sub-models and in the entirety of the domain regardless of the value of κ_0. Furthermore, drift terms require only a 'right-hand-side' evaluation, not temporal integration, and the cost of their evaluation is therefore independent of spatio-temporal variations in chemical stiffness. Since the monolithic model configurations do not incur an overhead cost attributed to model assignment, $\mathcal{L}_3 = 0$ in those cases. Lastly, we note that $\mathcal{L}_3$ varies with the constraint value [39] because of the iterative algorithm used to solve the assignment problem.

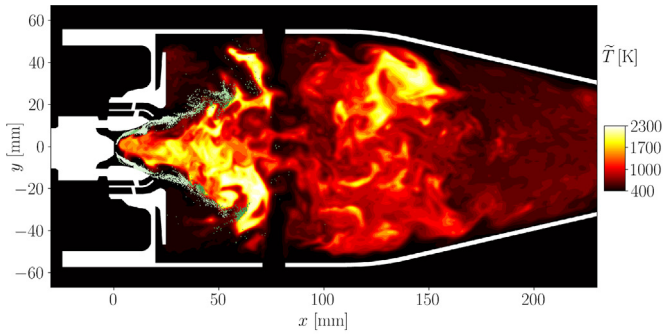

(a) Gas-phase temperature

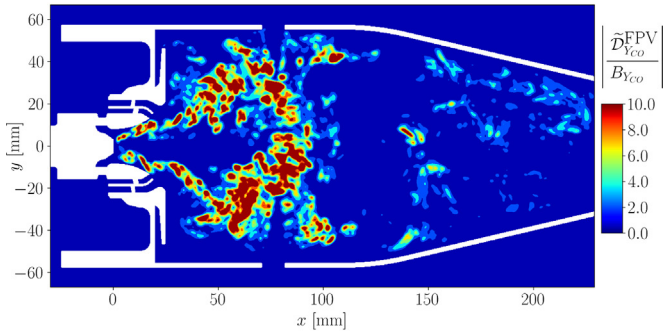

(b) Normalized absolute value of Y_{CO} drift term

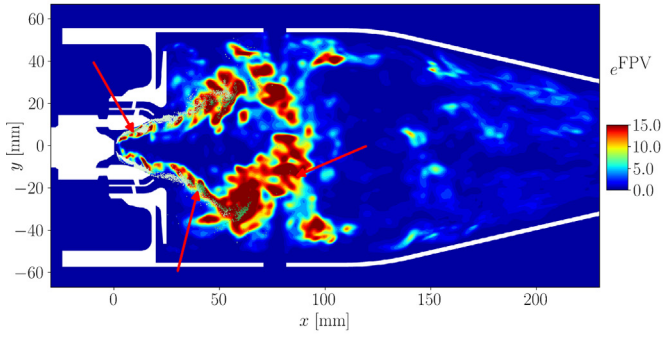

(c) Modeling error of the FPV sub-model

Fig. 5. A-priori analysis of a PEC0 simulation of the FAA Referee Rig combustor, shown instantaneously on the x, y plane. (a) and (c) show the spray present within 1 mm of the x, y plane. Arrows in (c) indicate key regions of FPV modeling error: the injector region, the flame brush and the first row of dilution holes.

5.1. A-priori analysis

To directly motivate the consideration of heterogeneous model assignment in the Referee Rig combustor, we assess the accuracy of the FPV sub-model when applied monolithically. We do so by employing the error-estimation methodology of the PEC framework in the limit of $\kappa = 0$, i.e., PEC0, such that there is no FRC assigned in the domain. The drift term, discussed in Section 3.1, provides a measure of the instantaneous deviation of a lower-fidelity sub-model from that of highest fidelity, in this case the deviation of FPV from FRC. Considering the QoIs discussed above, Eq. (17) then provides an instantaneous local error metric that can be used to assess the performance of the FPV sub-model, and in particular to determine which regions in physical space incur the largest modeling error from FPV. Similar a-priori analyses of the PEC framework have been applied successfully by Wu and Ihme [35] and Chung et al. [53] in other physical configurations.

In Fig. 5, we perform drift term and modeling error computations for a representative snapshot of a PEC0 simulation at steady state, and present the results on the $x-y$ plane. The temperature and spray fields are shown in Fig. 5(a) to provide context to the subsequent analysis. The figure shows the key aspects of the combustor discussed in Section 4.1, namely the highly swirled and turbulent flame in the primary zone, quenching by the first row of dilution holes and a lower temperature secondary zone. It is also evident that the spray extends from the injection point into the primary zone, interacting with the high-temperature gases of this region.

Figure 5 (b) shows the drift term for the CO mass fraction. The absolute value of the re-scaled quantity is presented, as this is the form in which the drift term enters the error metric in Eq. (17); see the discussion in Section 3.3. Although multiple QoIs are considered in this study, we find that their spatial distribution is similar and that the magnitude of the CO mass fraction drift term is largest, and hence we consider its analysis here. Considering the figure, it is apparent that $\widetilde{\mathcal{D}}^{\mathrm{FPV}}_{Y_{\mathrm{CO}}} \approx 0$ outside of the combustor and in the swirler passages. This is to be expected, since chemistry in these regions is inert. Of interest is that it can be seen that $\widetilde{\mathcal{D}}^{\mathrm{FPV}}_{Y_{\mathrm{CO}}} \approx 0$ in much of the secondary zone as well. This indicates that this highly fuel-lean region corresponds largely to equilibrated flamelets, and the tabulated and diffusion-flame-based FPV manifold is thus largely compliant to that of the topology-free FRC model. In the primary zone and the injector region, however, $\widetilde{\mathcal{D}}^{\mathrm{FPV}}_{Y_{\mathrm{CO}}}$ is significant, indicating substantial sub-model non-compliance.

To further assess the FPV sub-model, as well as to consider what effect applying the PEC framework will have on the solution, we consider the modeling error of the FPV sub-model in Fig. 5(c). The local error metric e^{FPV} is a scaled sum of drift terms for all QoIs per Eq. (18b), and is the dynamic quantity considered by the PEC framework's optimization algorithm for sub-model assignment through Eq. (23). Analysis of this field thus provides understanding of the sub-model assignment process. In the limit of $\kappa_0 = 0$, i.e., PEC0, there is no FRC assigned in the domain. As κ_0 is increased, the regions in the domain having the largest error metric will have highest priority to be assigned to the FRC sub-model. These are shown by red arrows in Fig. 5(c), corresponding (from left to right) to the injector region, the flame brush in the primary zone, and the quenching region near the first row of dilution holes. The first two regions have substantial spray evaporation, whereas the third undergoes a rapid change in composition due to the dilution jets. As was the case for $\widetilde{\mathcal{D}}^{\mathrm{FPV}}_{Y_{\mathrm{CO}}}$, $e^{\mathrm{FPV}} \approx 0$ in much of the secondary zone, indicating that it will only be assigned the FRC sub-model at large values of κ_0. The inert regions outside of the combustor have $e^{\mathrm{FPV}} = 0$, and will thus only be assigned to FRC as $\kappa_0 \to 1$, i.e., a monolithic FRC simulation. A key observation is that substantial FPV modeling error is only present for a relatively small portion of the combustor volume. This indicates that large values of κ_0 are unnecessary; only a small portion of the combustor (and thus a very small portion of the total domain) needs to be assigned to the FRC sub-model to achieve close compliance with the FRC manifold.

Further insight into the nature of the modeling error is obtained by considering its instantaneous scatter in $\tilde{T} - \tilde{Y}_{\mathrm{CO}}$ space in Fig. 6. We find that $e^{\mathrm{FPV}} \approx 0$ for all temperatures present within the domain when $\tilde{Y}_{\mathrm{CO}} \approx 0$. For higher temperature conditions with increased $\tilde{Y}_{\mathrm{CO}}$, we find that that the magnitude of e^{FPV} becomes significant, particularly for $\tilde{T} > 1500\,\mathrm{K}$ and $\tilde{Y}_{\mathrm{CO}} > 0.03$. Since $\tilde{Y}_{\mathrm{CO}}$ is an indicator of fuel-rich and non-equilibrium flame behavior, discrepancy in CO source term prediction between FPV and FRC is to be expected under these conditions. $\tilde{Y}_{\mathrm{CO}}$ is a key QoI, and thus from Eq. (5), discrepancy in the prediction of the CO source term results in significant FPV modeling error.

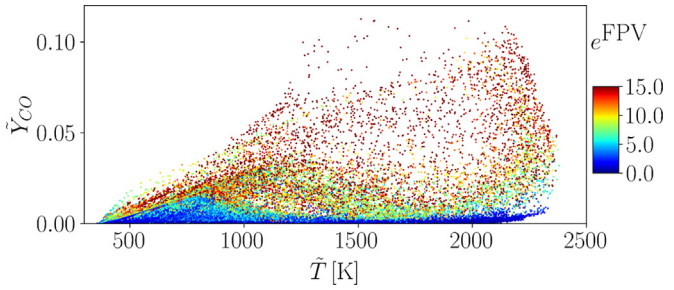

Fig. 6. Instantaneous scatter data of FPV modeling error from the a-priori analysis of a PEC0 simulation of the FAA Referee Rig combustor.

In Fig. 7, we provide visualizations of the instantaneous sub-model assignment field $\mathcal{M}$ at the time step considered in Fig. 5 for the three heterogeneous PEC model configurations considered in this study on the $x-y$ plane. Considering Fig. 7(a), we find that the FRC sub-model is indeed assigned to the three regions of highest FPV modeling error identified above, namely the injector region, the flame in the primary zone, and near the dilution jets. Comparing the boundaries of FRC sub-model assignment in Fig. 7(b), we see that as expected, a greater portion of the combustor is assigned to FRC with increasing cost constraint, with PEC6 and PEC11 encompassing most of the regions identified in Fig. 5(c) as having substantial FPV modeling error. The severe cost constraint in PEC1 limits FRC assignment to only a few small areas where modeling error is largest. For all model configurations considered, the outside of the combustor and the swirler passages are consistently assigned to IM, as expected from the a-priori analysis of the spatial distribution of the error metric.

5.2. Steady-state conditions

We proceed by considering the results of steady-state a-posteriori simulations. The objectives of the steady-state study are to demonstrate agreement with available gaseous and spray experimental data for both monolithic and heterogeneous model configurations, and to analyze the spatial distribution of the PEC sub-model assignment, since the latter is not possible in a transient simulation of LBO. The physical characteristics of the combustor at steady-state have been studied extensively by other authors [2,40,41,44,45], and we therefore do not repeat that analysis here; we limit our physical analysis to that of LBO in the subsequent section. Since we found in Section 5.1 that both PEC6 and PEC11 were able to achieve FRC sub-model assignment in most areas of substantial FPV modeling error, and that PEC1 did not, we perform PEC0 and PEC6 simulations at the steady-state condition of $\phi_g = 0.096$ for which experimental data is available. Statistics were collected over two flow-through times, corresponding to approximately 10 ms of physical time.

Given the complex flow physics of the experimental configuration considered, we assess first whether the correct gaseous flow behavior is recovered by the simulations, and to examine the sensitivity of the gaseous flow behavior to sub-model assignments. The average mass flow rate through the different combustor elements (i.e., swirlers, effusion holes and dilution holes) are compared to experimental measurements in Table 1. Results from PEC0 and PEC6 model configurations are in close quantitative agreement, indicating little sensitivity of these flow rates to the sub-model assignments in the combustor, as expected. Experimental measurements [2] were performed on a separate flowbench where the effective area of each component was measured by blocking all others. It was shown that this technique can result in some differences in the effective area of the swirler passages due to pressure coupling between the passages [2]. We find that the mass flow rates

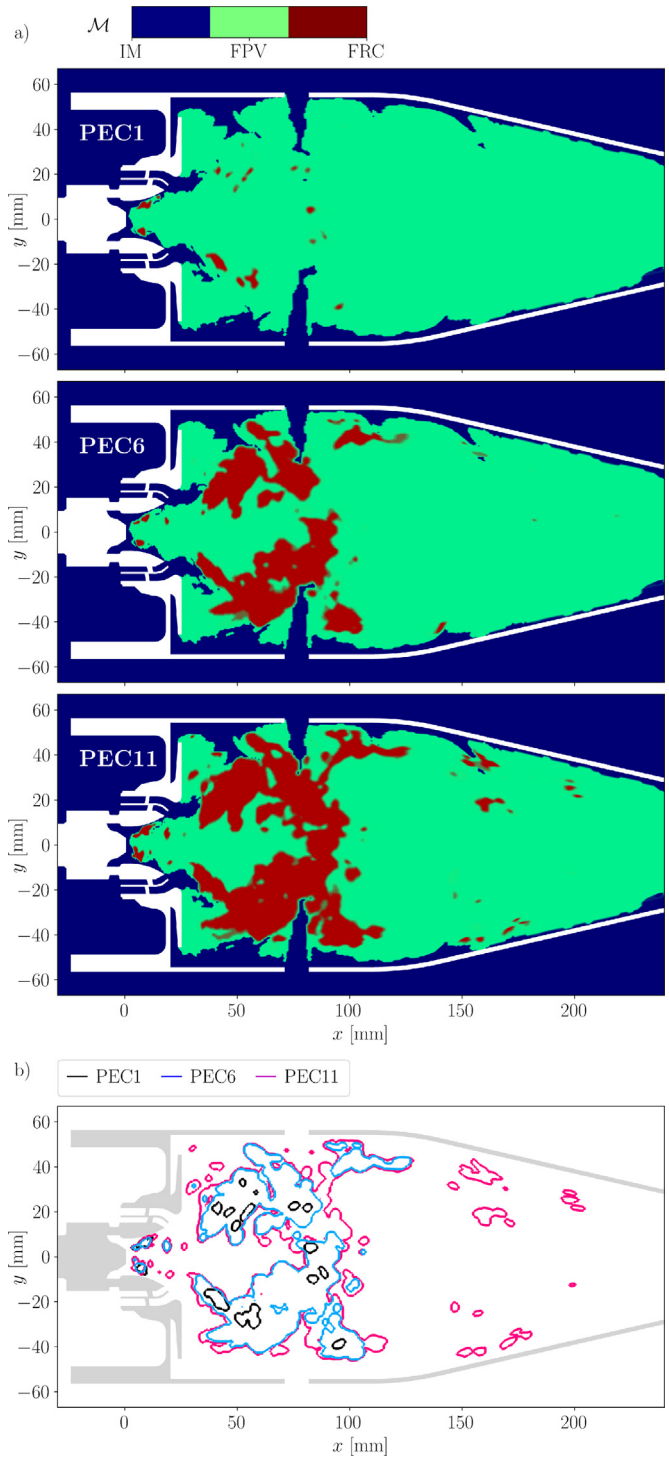

Fig. 7. Instantaneous sub-model assignments for the heterogeneous PEC model configurations. The full sub-model assignment fields are shown for each PEC model configuration in (a), and (b) shows the FRC sub-model assignment boundaries for all PEC model configurations.

through the effusion plates and dilution holes are in acceptable agreement with experiments. The flow split between the swirlers and dilution holes is also well predicted, meaning that the global equivalence ratio in the primary zone is expected to be well reproduced by the simulations. However, discrepancies in the mass flow split through the different swirler components are observed, reaching a maximum of 40% for the outer swirler. Esclapez et al. [2] showed that these differences can be partially attributed to the

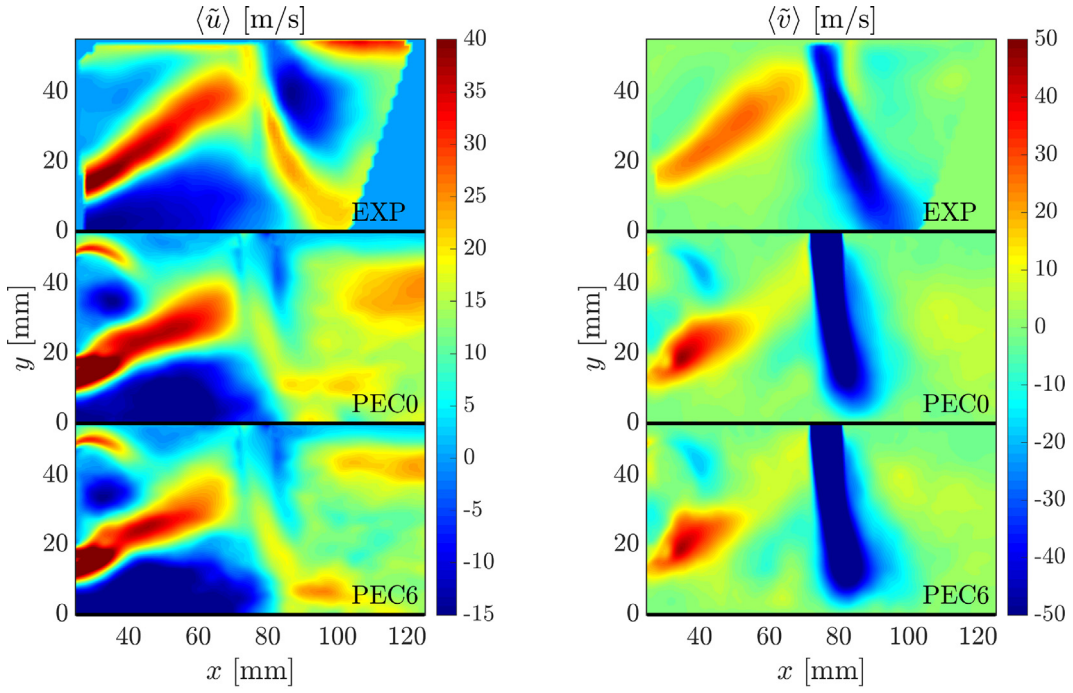

(a) Streamwise gas-phase velocity (b) Transverse gas-phase velocity

Fig. 8. Comparisons of PEC0 and PEC6 velocity fields with the PIV measurements of Rock et al. [54]. (a) and (b) show comparisons on the combustor centerplane for mean streamwise and transverse velocities, respectively.

Table 1
Comparison of experimental [2] and simulated mass flow rates (in g/s) through the swirlers (radial, internal axial and external axial), effusion boundaries and dilution holes. The relative standard deviation of experimental results is also provided.

	Experiments	PEC0	PEC6
Radial swirler	14.3 ± 5.1%	10.4	10.6
Int. axial swirler	18.9 ± 10.0%	24.3	24.2
Ext. axial swirler	24.6 ± 13.0%	34.5	34.3
Total swirler	60.7 ± 1.5%	69.2	69.0
Effusion	245.4 ± 0.9%	247.1	247.1
Dilution row 1	39.5 ± 2.0%	37.6	37.8
Dilution row 2	45.4 ± 1.5%	40.3	40.2

under-resolution of the boundary layer in the swirler vanes and the effect of the SGS model.

To verify that the discrepancies in the swirler mass flow rates do not significantly affect the gas-phase flow in the combustor, we perform further comparisons to PIV data obtained by Rock et al. [54]. Figure 8(a) and (b) show the mean streamwise and transverse velocity fields, $\langle\tilde{u}\rangle$ and $\langle\tilde{v}\rangle$, on the combustor centerplane. These show that the flow field's global features are qualitatively well-captured by the simulations, with little sensitivity to the PEC model configuration. The swirling annular jet impinges on the base of the dilution holes, leading to a streamwise deviation of the dilution jets. An inner recirculation zone is created, which stabilizes the flame in the primary zone. Figure 8(a) and (b) quantitatively compare the flow fields at several streamwise locations, which are in reasonable agreement up to $x = 45$ mm. Figure 9(a) also shows flow statistics for the PEC0 model configuration after four flow-through times (approximately 20 ms). The close quantitative agreement of the statistics after two and four flow-through times across multiple locations in the combustor is indicative of the statistical convergence of the results presented in this section. The location of maximum streamwise and transverse velocity shows that the spreading rate is well captured by the LES in both PEC model configurations considered. The bulkhead flow at the top left of the panels in Fig. 9(a) and (b) and the regions near the dilution holes show discrepancies with experimental results. However, none of these inlets were seeded with particles in the PIV, thus leading to greater uncertainty in the measurements in these regions [54]. These results show that the effect of the mass flow split differences noted above are not substantial in the region immediately downstream of the swirlers' exit, and agreement in other regions is acceptable in light of the experimental uncertainties present.

We now verify the simulated behavior of the fuel spray, given the key role it plays in determining the flame dynamics [55–57]. Figure 10 shows droplet size distributions obtained from experiments and simulations at the location $(x, y) = (25\,\text{mm}, 15\,\text{mm})$. This position is downstream of the SBU region (near $x = 5$ mm), and at the boundary between the injector region and the primary combustion zone. The polydisperse droplet injection considered in the simulations employs a Rosin–Rammler distribution with a Sauter mean diameter of 56 µm, discussed in detail by Esclapez et al. [2] and shown by the dashed line in the figure. Comparing the downstream droplet distributions to the injected distribution, it can be seen that the mean droplet size has significantly decreased due to SBU and evaporation. In particular, all droplets with a diameter greater than 50 µm have broken into smaller ones. The discrepancy between the simulated results is small, which is expected as all simulations employ the same SBU and droplet evaporation models. The black line in Fig. 10 shows the droplet size distribution from measurements performed at cold-flow conditions, reported in Esclapez et al. [2]. Details of the spray diagnostics employed are discussed by Bokhart et al. [58]. While small-size droplets are more frequent in the experiments, the most probable droplet diameter d_{mp} is similar between experiments and simulations. The maximum distribution value and corresponding droplet diameter differ by approximately 30% and 10%, respectively, between the numerical and experimental results. However, some discrepancies between the cold-flow experiments and reacting simulation results are expected, especially for small droplets. This is

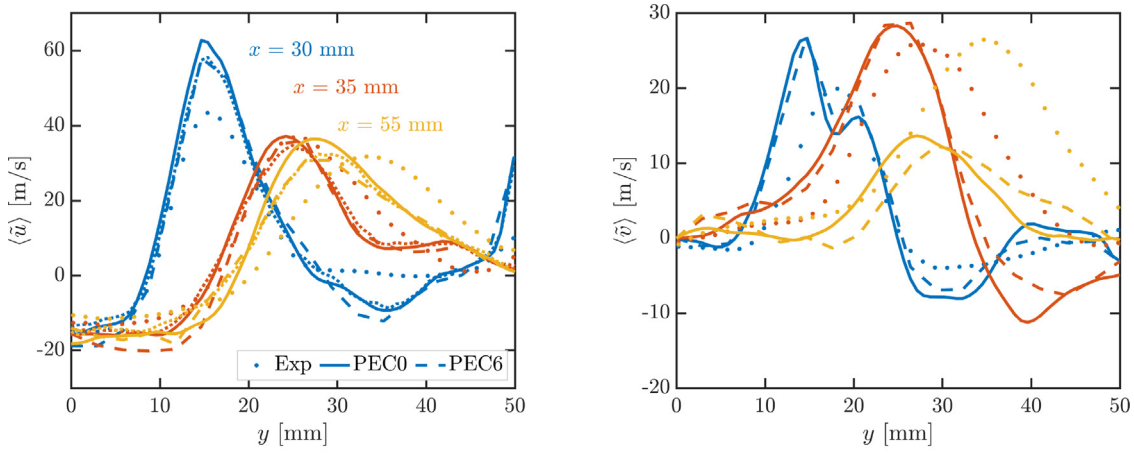

(a) Streamwise gas-phase velocity (b) Transverse gas-phase velocity

Fig. 9. Comparisons of PEC0 and PEC6 velocity profiles with the PIV measurements of Rock et al. [54]. (a) and (b) provide quantitative comparisons at different streamwise locations for the streamwise and transverse velocities, respectively. The dotted lines in (a) show the flow statistics for the PEC0 model configuration after four flow-through times.

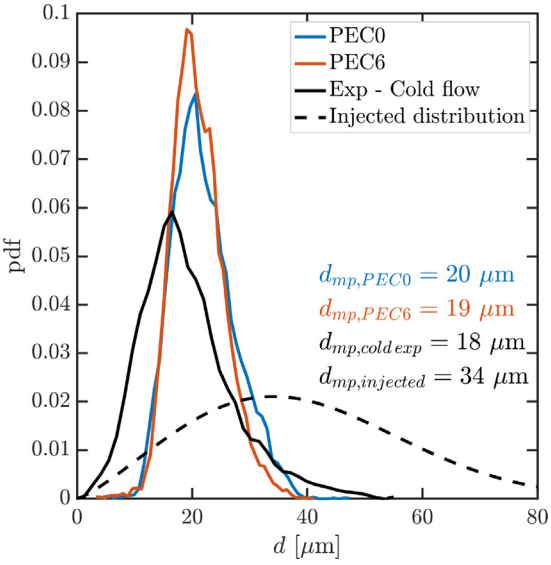

Fig. 10. Droplet size distributions. Solid lines show results from simulations and experiments at the location $(x, y) = (25\,\text{mm}, 15\,\text{mm})$. The dashed line indicates the injected distribution.

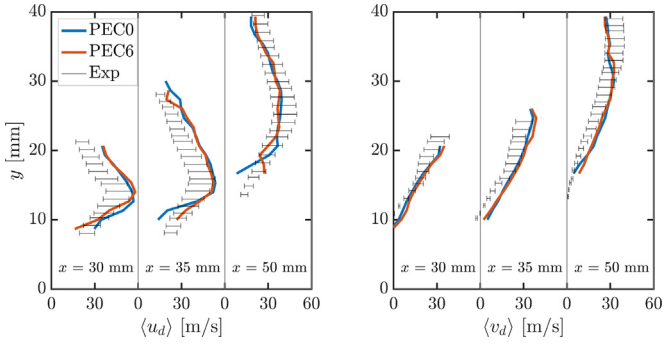

Fig. 11. Mean streamwise and transverse spray velocities from numerical and experimental [2] results.

because in the simulations, higher temperatures near the injector from recirculated gases result in higher droplet evaporation rates, causing the observed narrowing of the distribution toward larger values of d.

To verify the spatio-temporal development of the fuel spray after injection, we compare spray velocity statistics at different streamwise locations in Fig. 11. Simulation results are again similar for both PEC model configurations, as expected since the simulations employ the same droplet drag and evaporation models discussed in Section 2. Furthermore, the velocity field results, shown in Figs. 8 and 9, indicate that the feedback of combustion sub-model assignments on the flow field is limited in this system, resulting in similar spray-gas momentum coupling across simulations. We find that the simulations are able to adequately reproduce the spray angle and the magnitude of the axial and radial velocity components.

The agreement achieved for both spray and gas-phase velocity fields shows that the present two-way coupled Eulerian–Lagrangian formulation adequately captures the multiphase flow physics of the Referee Rig combustor. We note also that this assessment is an important capability of the PEC framework: we have demonstrated that in the present physical configuration, the magnitudes and spatial distributions of the steady-state gaseous and spray velocities have limited sensitivity to the combustion model assignment. The PEC framework allowed us to make this assessment without incurring the substantial computational cost of performing a monolithic FRC simulation that would otherwise be necessary to compare to the results of our monolithic PEC0 simulation.

We now investigate how the FPV sub-model results in modeling error, and how the PEC framework performs sub-model assignments to mitigate this. In the first column of Fig. 12(a), we consider the temporally-averaged local error field $\langle e^{\text{FPV}} \rangle$ for both PEC0 and PEC6 model configurations. We find $\langle e^{\text{FPV}} \rangle$ is substantial in the regions identified in the a-priori analysis, with the injector region and in the primary zone near $(x, y) = (40\,\text{mm}, 25\,\text{mm})$ having the largest values. A key observation is that with increasing value of the cost constraint, the spatial distribution of $\langle e^{\text{FPV}} \rangle$ stays nearly constant, but decreases in magnitude by up to a factor of three from PEC0 to PEC6. This is direct evidence that through targeted assignment of the FRC sub-model to locations where FPV is inadequate, with the severity of its inadequacy judged using $\langle e^{\text{FPV}} \rangle$, the PEC framework has improved not only the compliance of the overall solution with the FRC manifold, but also that of the FPV sub-model.

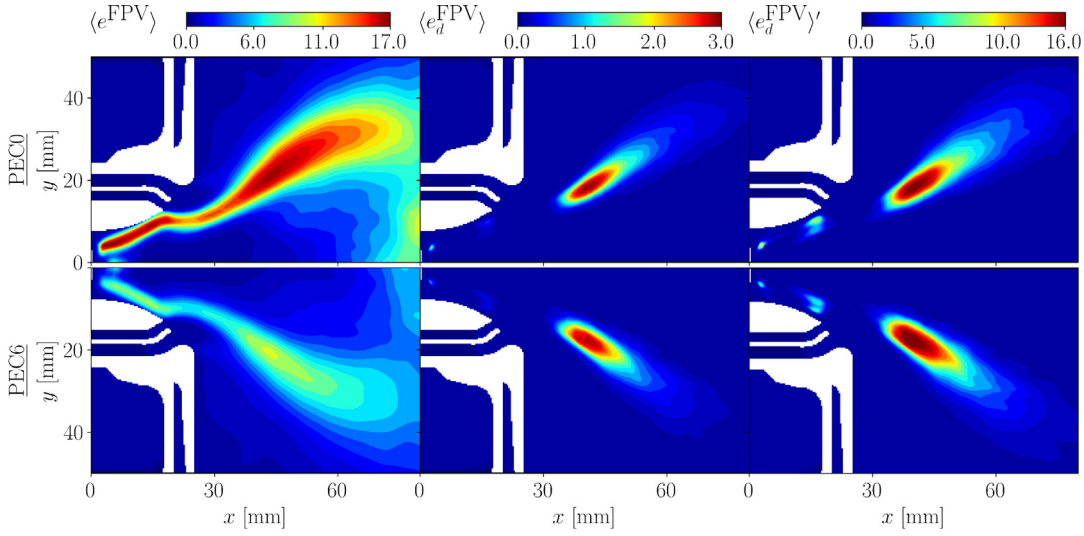

(a) Error metrics used in the PEC framework for sub-model assignment.

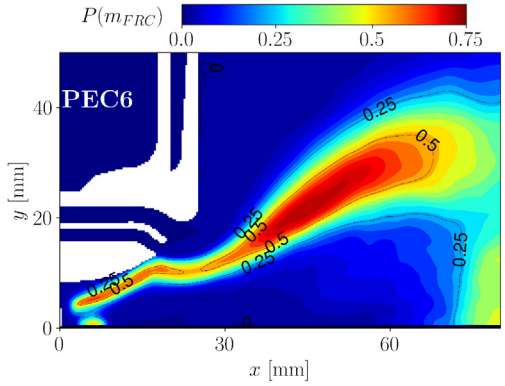

(b) Model assignment of the PEC framework, expressed as the probability of assigning the FRC sub-model. Labeled iso-lines indicate sub-model assignment probability iso-contours.

Fig. 12. Temporally-averaged modeling error metrics and associated sub-model assignment for steady-state operating conditions, $\phi_g = 0.096$.

In the context of spray combustion, we can define the spray contribution to the local error using $\widetilde{\mathcal{D}}^m_{\psi,d}$ as

$$e_d^m = \sum_{\psi \in Q} \left| \frac{\widetilde{\mathcal{D}}^m_{\psi,d}}{B_\psi} \right|. \tag{24}$$

We present the temporally averaged field $\langle e_d^{\mathrm{FPV}} \rangle$ in the second column of Fig. 12(a), from which we find that the spray contributes most significantly to modeling error in the primary zone near $(x, y) = (40\,\mathrm{mm}, 25\,\mathrm{mm})$. Its peak root-mean-square (RMS) value $\langle e_d^{\mathrm{FPV}} \rangle'$, shown in the third column of Fig. 12(a), is of the same magnitude as the peak value of $\langle e^{\mathrm{FPV}} \rangle$. This shows that although the mean values of e_d^{FPV} are small compared to those of e^{FPV}, its instantaneous local contribution can be substantial. As noted in Section 3.2, spray contribution to drift terms, and consequently modeling error, are significant during spray-flame interaction due to increased chemical sensitivity and evaporation rates. Given the highly turbulent swirling gaseous flow and the stochastic nature of droplet injection trajectories and breakup, spray-flame interaction in the primary zone is expected to be highly intermittent, leading to large values of $\langle e_d^{\mathrm{FPV}} \rangle'$.

We note that despite the reduction in $\langle e^{\mathrm{FPV}} \rangle$ achieved through targeted FRC assignment from PEC0 to PEC6, the magnitudes and spatial distributions of $\langle e_d^{\mathrm{FPV}} \rangle$ and $\langle e_d^{\mathrm{FPV}} \rangle'$ remain nearly constant. This is because FPV is unable to capture certain effects of finite-rate chemistry and spray evaporation due to its model assumptions, as discussed in Section 1. The FPV manifold is non-compliant with the FRC manifold during direct spray-flame interaction. Thus, even in a monolithic FRC simulation where $\kappa_0 \to 1$, the FPV manifold will be non-compliant with the FRC manifold in some parts of the domain, and e^{FPV} will remain finite in those regions.

Sub-model assignment achieved through the PEC framework is considered statistically in Fig. 12(b) through the probability of assigning the FRC sub-model, $P(m_{FRC})$. We do so since in the present highly turbulent and swirled flow, the flame is corrugated and dynamic, causing the spatial sub-model assignment topology to adapt continuously. As expected, most locations in the injector region and primary zone with high values of $\langle e^{\mathrm{FPV}} \rangle$ have the highest probabilities of assignment to the FRC sub-model, with more than 50% FRC assignment probability in the injector region along the spray injection trajectory.

A key observation is that $P(m_{FRC})$ exceeds 60% in the primary zone near $(x, y) = (40\,\mathrm{mm}, 25\,\mathrm{mm})$, which coincides with the re-

gion where $\langle e_d^{\mathrm{FPV}} \rangle$ is maximum. Thus the PEC framework most consistently assigns FRC to locations with direct spray-flame interaction. This is because of the above-noted non-compliance of FPV with the FRC manifold during direct spray-flame interaction, which persists irrespective of the cost constraint considered. The PEC framework must therefore consistently assign FRC to locations with direct spray-flame interaction in order to minimize overall modeling error. By contrast, in regions where $\langle e_d^{\mathrm{FPV}} \rangle \approx 0$, a limited amount of FRC assignment brings the FPV manifold into closer compliance with that of FRC, thus necessitating statistically less FRC assignment in those regions.

5.3. Lean blow-out

We now consider the effect of the spray-augmented PEC framework in predicting the transient phenomenon of LBO. To allow direct comparisons of the LBO results, simulations are started from the same steady-state solution obtained from a PEC0 simulation and the global equivalence ratio is changed instantaneously from $\phi_g = 0.096$ to $\phi_g = 0.077$. As discussed in Section 4.1, all boundary conditions are held constant except the liquid fuel mass flow rate. Four simulations are performed under these conditions with different PEC model configurations: PEC0, PEC1, PEC6 and PEC11. Motivated by the a-priori analysis of Section 5.1, these model configurations were chosen to demonstrate the sensitivity of the macroscopic combustor behavior to limited increases in user-specified cost.

Results of all model configurations are compared qualitatively in physical space in Fig. 13, in mixture fraction space in Fig. 14, and in $\tilde{T} - \tilde{Y}_{\mathrm{CO}}$ space in Fig. 15. Quantitative comparisons are made in Fig. 16, and videos of the PEC1 and PEC6 LBO simulations in physical space are provided as supplementary material. We note that because all species mass fractions are transported in FRC whereas in IM and FPV they are obtained via table look-up, the values of $\langle Y_{\mathrm{OH}} \rangle$ at $t = 0$ ms in Fig. 16 differ among the PEC model configurations. This is unlike mixture fraction, which is a conserved quantity, and temperature, which is obtained from conserved quantities, and are therefore identical among PEC model configurations at $t = 0$ ms. Considering the transient behavior of the temperature field in Fig. 13(a), we see that in all simulations, temperature first reduces in the secondary zone as the lean-burn region of the combustor extinguishes, followed by the primary zone. The secondary zone is highly fuel-lean during steady operation, and thus after the fuel flow rate is reduced to induce LBO, combustion in this region becomes unsustainable. This is seen most clearly in the composition space analysis of Fig. 14, where the third row of each subfigure shows the instantaneous state of the secondary zone. Initially, the scatter follows a near-equilibrium burning flamelet solution from pure oxidizer to near-stoichiometric conditions. After the fuel flow rate is reduced, the instantaneous scatter is seen to recede at a similar rate for all model configurations to lower temperatures and leaner mixture fractions. However, we find that temperature in the primary zone, a key indicator of LBO, reduces more rapidly with the PEC6 and PEC11 model configurations than PEC0 and PEC1. This is shown quantitatively in Fig. 16(a), where the rate of average temperature reduction in the primary zone using the PEC6 and PEC11 model configurations is found to be three times that of PEC0. Considering the primary zone in composition space in the second row of Fig. 14, we see that PEC0 in particular retains a flamelet structure even up to $t = 6.0$ ms, whereas in the PEC6 and PEC11 simulations the primary zone has become almost entirely fuel-lean by $t = 3.1$ ms, with near-complete blow-out by $t = 6.0$ ms. The flame structure in the primary zone of the PEC1 simulation is similar to that of PEC0, but recedes to $\tilde{Z} < 0.08$. The rate of average temperature reduction in the primary zone is also greater than PEC0, at approximately -19 K/ms for PEC1, compared to -15 K/ms for PEC0. In all model configurations, we see an increase in fuel-lean and near-stoichiometric scatter data for $\tilde{T} < 1000$ K, indicating an expected reduction in reactivity as LBO progresses.

To analyze reasons for the difference in blow-out behavior of the different PEC model configurations, we consider the OH mass fraction and progress variable fields in Fig. 13(b) and (c), respectively. As blow-out progresses, PEC6 and PEC11 predict a rapid reduction in $\tilde{Y}_{\mathrm{OH}}$ in the injector region, with little present at $t = 3.1$ ms. By $t = 6.0$ ms, $\tilde{Y}_{\mathrm{OH}}$ levels are insignificant throughout the combustor and $\tilde{C}$ is reduced substantially, indicating a near-complete extinction of the flame. Considering the transient PEC0 behavior, we find that at $t = 6.0$ ms the values of $\tilde{Y}_{\mathrm{OH}}$ and $\tilde{C}$ remain high inside the injector region, as well as the primary zone. The difference in the rate of average $\tilde{Y}_{\mathrm{OH}}$ reduction in the primary zone is shown quantitatively in Fig. 16(b), from which we see that $\langle \tilde{Y}_{\mathrm{OH}} \rangle$ approaches zero at approximately $t = 6.5$ ms for PEC6 and PEC11 simulations, but remains significant in the PEC0 simulation beyond $t = 13.0$ ms.

The preceding analysis has shown that PEC0 predicts a significantly more stable flame than the heterogeneous PEC model configurations. We can understand the physical nature of this stabilization by considering the injector region in composition space, shown in the first row of each subfigure in Fig. 14. From Fig. 14(a), we see that as LBO progresses, the injector region transitions from a fuel-lean and near-stoichiometric structure to a fully-burning flamelet structure spanning lean and rich compositions. Since the injector region is immediately upstream of the primary zone, the hot products of the injector region stabilize combustion in the primary zone, significantly slowing down the blow-out process. The PEC1 simulation results shown in Fig. 14(b) exhibit similar behavior, but are limited to leaner compositions and lower temperatures than PEC0. By contrast, in the PEC6 and PEC11 simulations shown in Fig. 14(c) and (d), the injector region extinguishes rapidly, with $\tilde{Z} < Z_{st}$ and $\tilde{T} < 1500$ K by $t = 6.0$ ms. The reduction in reactivity, heat release and therefore temperature in the primary zone reduce the rate of spray vaporization, resulting in a reduction in average mixture fraction, as shown in Fig. 16(c). The feedback loop of fuel vapor production and consumption required for steady spray combustion is thus broken, thereby ensuring a complete blow-out of the flame.

We analyze the transient sub-model assignment behavior in composition space to gain a better understanding of the thermochemical conditions under which PEC performs model assignments. In Fig. 14, we find that the states corresponding to the mixing line and to equilibrium flamelet behavior are consistently assigned to IM and FPV, respectively. As expected, IM and FPV are assigned to those states where they perform best in terms of discrepancy of QoI source term predictions with FRC. Increasing κ_0 results in a greater number of the non-equilibrated burning states to be assigned to FRC, conditions under which the discrepancy between FPV and FRC is greatest. Further insight is gained by considering Fig. 15, where instantaneous scatter data from the primary zone of the combustor is presented in $\tilde{T} - \tilde{Y}_{\mathrm{CO}}$ space. In Section 5.1, we considered instantaneous PEC0 results from the steady-state condition, and showed that the FPV modeling error was most significant for $\tilde{T} > 1500$ K and $\tilde{Y}_{\mathrm{CO}} > 0.03$. Similarly, we find for the present results that at $t = 0.0$ ms, increasing κ_0 results in a greater portion of those states being assigned to the FRC sub-model. As LBO progresses, the PEC0 and PEC1 model configurations retain similar structures over time, with moderate reductions in $\tilde{T}$ and $\tilde{Y}_{\mathrm{CO}}$. The PEC6 and PEC11 model configurations exhibit a more rapid and substantial reduction in these quantities, as expected given their more rapid blow-out. Comparing Figs. 15 and 14, we find that by $t = 6.0$ ms, much of the FRC sub-model assignments in the primary zone correspond to highly non-equilibrated burning states with $\tilde{T} < 1500$ K, but still significant $\tilde{Y}_{\mathrm{CO}}$. These are conditions un-

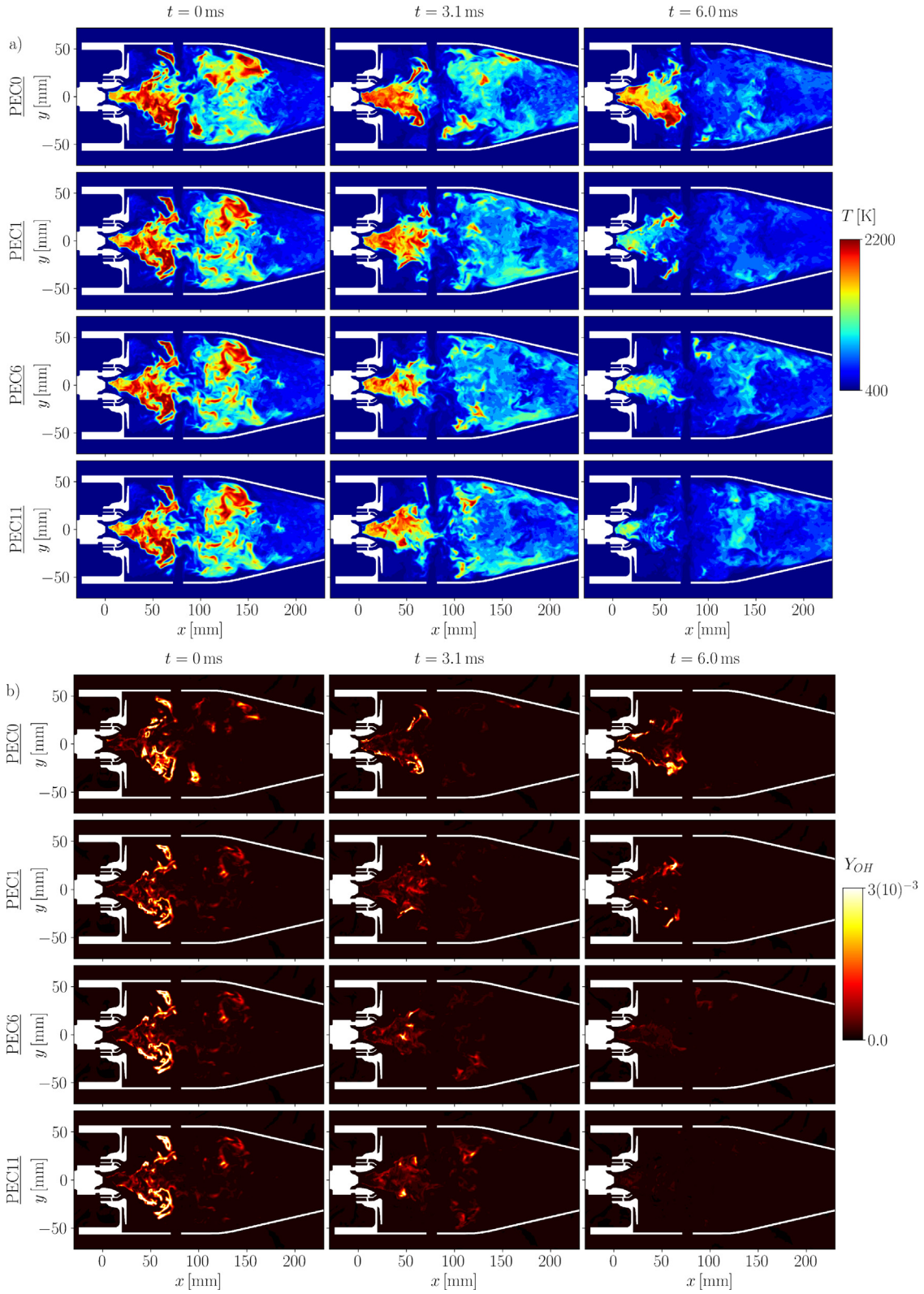

Fig. 13. Transient combustor behavior during LBO for all model configurations. $t = 0$ ms refers to the time step before ϕ_g was changed from the steady-state value of 0.096 to 0.077.

der which the FPV manifold is in substantial disagreement with FRC, with the associated large FPV modeling errors resulting in FRC assignment by the PEC framework.

We now consider how changes in the PEC model configuration result in different levels of flame stabilization. During the process of LBO, the PEC model dynamically adapts the sub-model assignments to changes in the flame distribution in the combustor. This is shown by the model assignment $\mathcal{M}$ in physical space in Fig. 13(d). We find that FRC is assigned primarily to the regions identified in Section 5.1 as having the largest FPV modeling er-

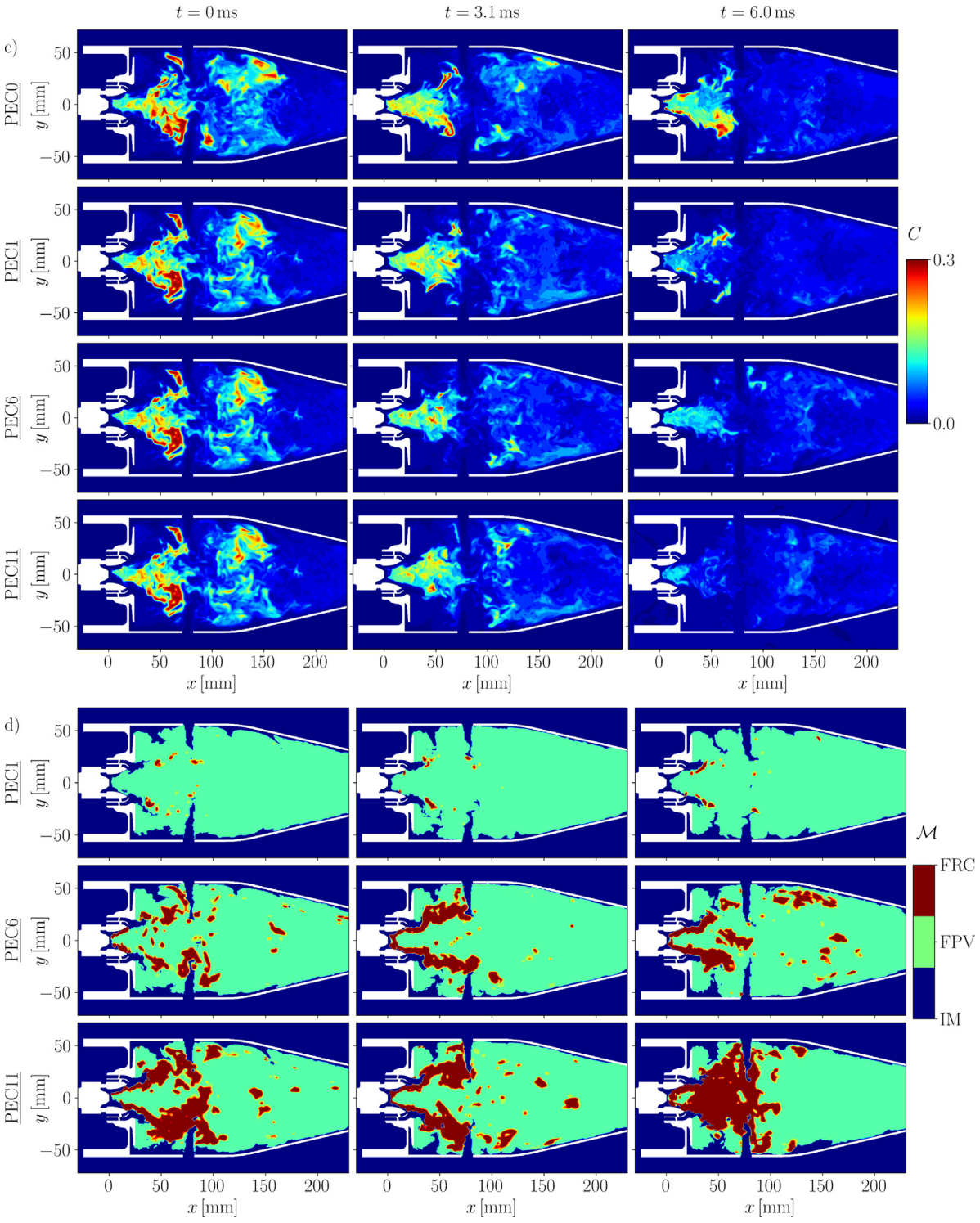

Fig. 13. Continued

ror: the injector region, along the flame brush in the primary zone and near the first row of dilution holes. As was the case in the steady-state results in Section 5.2, the plenum region outside the combustor, the swirlers and the dilution jets correspond to IM. In light of Figs. 13 and 14, comparing the behavior of the PEC6 and PEC11 model configurations with that of PEC0, we find that when applied monolithically, the FPV sub-model predicts that thermochemical states present in the injector region at the start of LBO allow for flame stabilization there. As was the case in the a-priori analysis of Section 5.1 and the steady-state results of Section 5.2, we find that the PEC framework identifies this region as one of large FPV modeling error, resulting in a significant portion of the injector region being assigned to FRC in the PEC6 and PEC11 model configurations. We thus find that the FRC sub-model predicts that the thermochemistry of the injector region precludes flame stabilization, limiting the flame to the primary zone. Therefore, in the PEC0 model configuration the magnitude of the reduction in fuel vapor production is smaller, ultimately resulting in a substantially

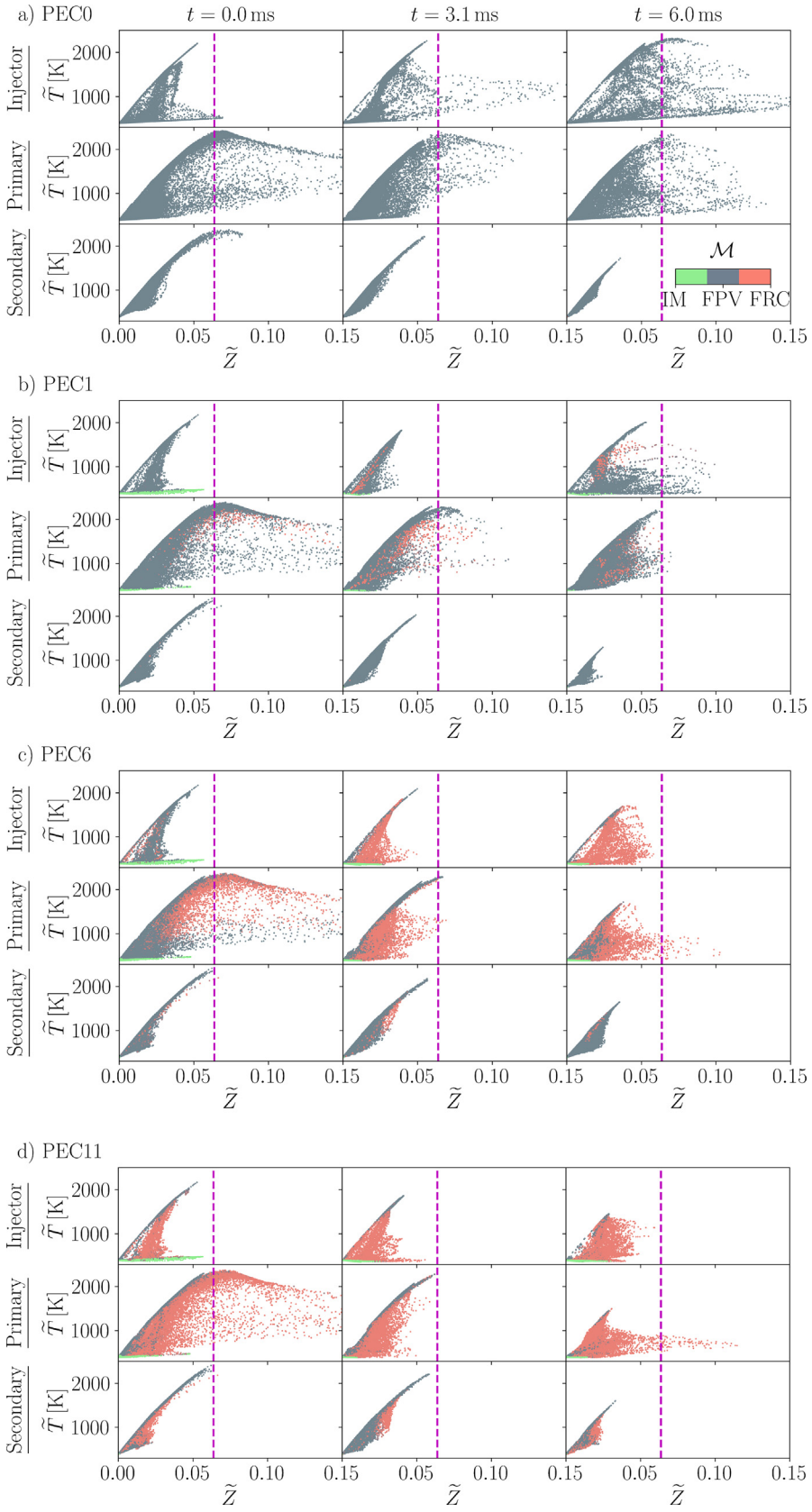

Fig. 14. Instantaneous scatter data of transient combustor behavior during LBO for all PEC model configurations. The labels 'Injector', 'Primary' and 'Secondary' refer to the injector region, primary zone and secondary zone of the combustor, as identified in Fig. 3. Scatter data is colored by PEC sub-model assignment $\mathcal{M}$.

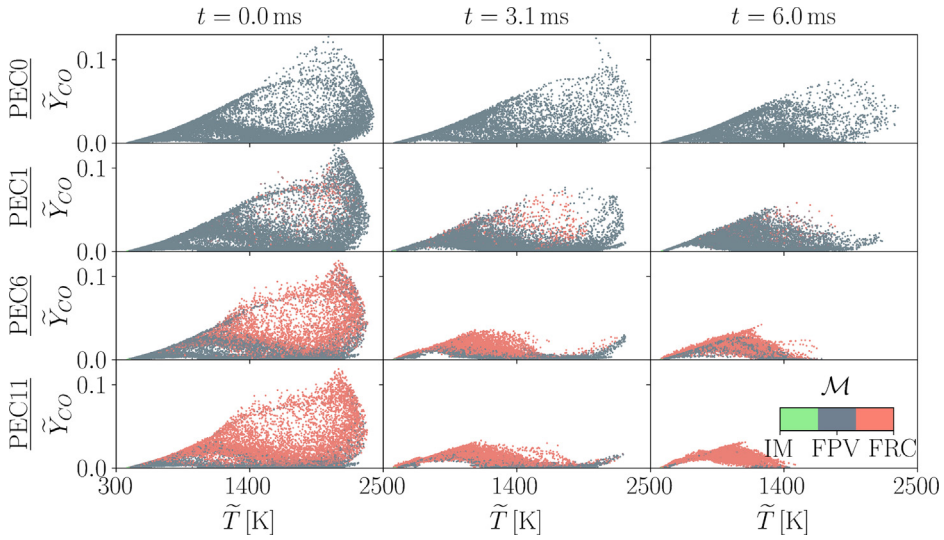

Fig. 15. Instantaneous scatter data from within the primary zone of the combustor during LBO for all PEC model configurations. Data is plotted in temperature-CO mass fraction space and is colored by PEC sub-model assignment $\mathcal{M}$.

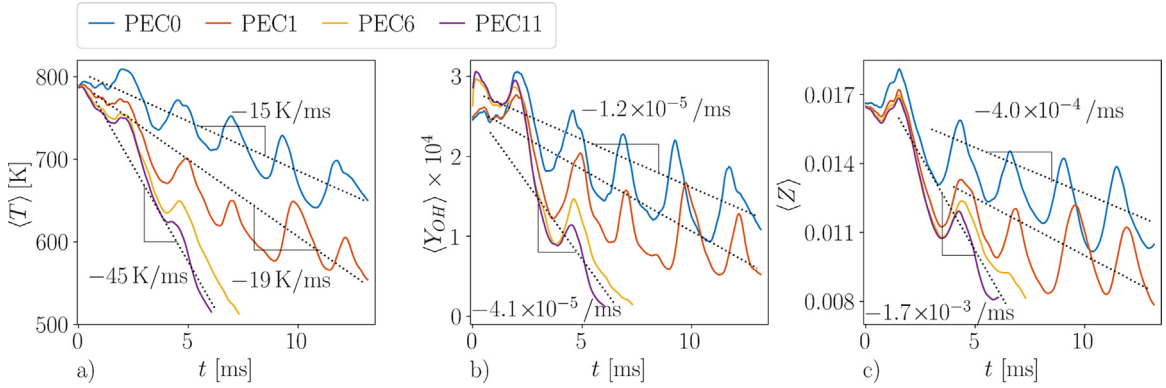

Fig. 16. Quantitative comparisons of all model configurations during LBO for variables spatially averaged in the primary zone. $t = 0$ ms refers to the time step before ϕ_g was changed from the steady-state value of 0.096 to 0.077.

slower blow-out prediction and indicating an over-prediction of flame stability against LBO. It is noteworthy that throughout the process of LBO, although the secondary zone is undergoing extinction, we find that most of the FRC sub-model assignment remains in the injector region and primary zone, and not in the secondary zone. This is seen most clearly in Fig. 14, where we find that for all PEC model configurations, much of the scatter in the secondary zone corresponds to equilibrium flamelet behavior and is assigned to the FPV sub-model. The fuel-lean extinction of the secondary zone is thus relatively well-captured by the FPV sub-model compared to the combustion dynamics of the upstream regions, as was identified in Section 5.1.

It is of interest to observe that in the volume-averaged primary zone results of Fig. 16, the PEC6 and PEC11 model configurations are quantitatively similar in their transient blow-out behavior. The rates of reduction in average primary zone temperature, OH mass fraction and mixture fraction differ by less than 5%. Transient simulations magnify differences between model configurations, since a difference in local sub-model assignment at one time step will be compounded by subsequent sub-model assignments that rely upon local source term evaluations. Thus, the close quantitative agreement for volume-averaged quantities achieved between PEC6 and PEC11 model configurations is an indication of the convergent behavior of the PEC framework's prediction of macroscopic combustor dynamics with respect to the cost constraint. The PEC6 and PEC11 model configurations assign sufficient FRC to the injector region so as to recover the reduced stability of the primary zone, resulting in close agreement of volume-averaged quantities during LBO. By contrast, PEC1 is unable to assign sufficient FRC to prevent flame stabilization in the injector region due to the severe cost constraint, as seen in Fig. 13(d), and therefore predicts similar stabilization behavior to PEC0, with quantitative results lying between those of PEC0 and PEC6/PEC11. Thus, similarly to the discussion of the sensitivity of velocity fields to combustion modeling in Section 5.2, we find that the PEC framework allows the isolation and identification of the sensitivity of transient combustor behavior to the combustion sub-models employed, without incurring the substantial computational cost of a monolithic FRC simulation.

We consider lastly an analysis of the numerical performance achieved by the sub-model assignment algorithm during transient simulations. From Eq. (23), we see that since the optimization algorithm relies upon an inequality constraint on the normalized cost κ_0 to achieve model assignment, the normalized cost is not guaranteed to be precisely the assigned value. It is therefore of interest to consider the normalized cost achieved by the PEC framework, κ, over time. As discussed in Section 3.3, for the sub-models considered in this study, κ corresponds closely to the portion of the control volumes in the combustor assigned to the FRC sub-model. Considering temporal variation in κ is most relevant during globally transient simulations, such as the present analysis of

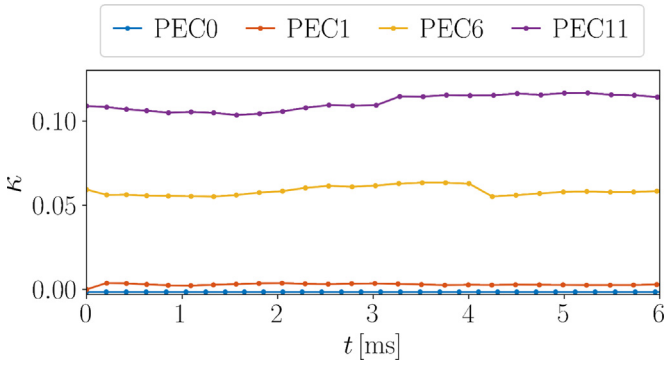

Fig. 17. Time trace of κ during blow-out simulations, which in the present study corresponds to the percentage of control volumes within the combustor assigned to the FRC sub-model.

LBO, since the sub-model assignment algorithm must perform significant adaptation of the sub-model assignment topology to attain the desired constraint value κ_0. This is in contrast to the previous formulation of the optimization problem employing a Lagrange multiplier λ, Eq. (19), which could not enforce a cost constraint in a globally-transient simulation like that of LBO due to the nature of the formulation, as discussed in Section 3.3. In Fig. 17, we find that despite some temporal variation, κ is reasonably stable, showing that the PEC framework presented in this study is able to achieve constant-cost simulation of LBO. This further demonstrates utility of the present formulation for both steady and transient simulations of multiphase turbulent combustion.

6. Conclusions

The PEC framework for dynamic combustion sub-model assignment was extended to spray combustion through a rigorous analysis of the governing equations. We showed that spray affects the drift terms used for sub-model assignment when both the local rate of fuel vapor production and the gas-phase chemical sensitivity are significant, conditions which are present during spray-flame interaction. To provide direct user control of simulation cost, we re-posed the model-assignment problem as a cost-constrained optimization problem instead of using a relative weighting of cost and error. To demonstrate the effectiveness of the spray-augmented PEC formulation in modeling turbulent multiphase combustion in practical systems where the use of a monolithic FRC model with realistic chemistry is precluded by excessive computational cost, we performed a series of simulations of the FAA Referee Rig combustor. We used the extended definition of the drift term as a standalone metric to evaluate modeling error in an a-priori analysis. This identified three principal regions of FPV modeling error, namely the injector region, along the flame brush in the primary zone and near the first row of dilution holes. We compared results of both monolithic and heterogeneous simulations to a number of experimentally measured quantities at steady-state conditions and achieved satisfactory agreement. Consideration of the statistical results for FPV modeling error and PEC sub-model assignment showed that the PEC framework's judicious assignment of the FRC sub-model resulted in improved compliance of the FPV manifold with that of FRC. We found that the non-compliance of the FPV model arising from spray-flame interaction was not improved by FRC assignment due to the modeling assumptions of the former, and the PEC framework therefore assigned FRC to regions of significant spray-flame interaction with the highest probability. To assess model behavior in transient cases, LBO simulations were performed with the four model configurations: PEC0, PEC1, PEC6 and PEC11, where PEC0 corresponds to a monolithic FPV simulation. We found that in the PEC0 model configuration, the FPV sub-model over-predicted reactivity in the injector region, resulting in an over-prediction of flame stability and a significantly slower blow-out compared to the heterogeneous simulations. The PEC6 and PEC11 model configurations achieved quantitatively similar transient results, demonstrating the rapid convergence of the transient combustor behavior with respect to the cost constraint. This study has shown that the spray-augmented PEC formulation is a computationally-efficient means of improving the fidelity of simulations of multiphase turbulent combustion in practical systems at a reduced computational cost, transferring direct control of simulation cost and accuracy to the user. It has further been shown to be an effective tool for evaluating the sensitivity of simulation results to the combustion models employed and analyzing the physical causes for that sensitivity.

Declaration of Competing Interest

The authors declare that they have no known competing financial interests or personal relationships that could have appeared to influence the work reported in this paper.

Acknowledgments

Financial support from NASA under grant number NNX15AV04A, NAVAIR under contract number N68335-19-C-0177 and The Boeing Company under grant number 134708 [IC2017-2182] is gratefully acknowledged. This research used resources of the National Energy Research Scientific Computing Center, a U.S. Department of Energy Office of Science User Facility operated under Contract no. DE-AC02-05CH11231.

Appendix A. Demonstration of modeling error metrics in a steady one-dimensional wall-stagnating spray flame

To clearly illustrate the behavior of the gaseous and spray components of the modeling error metric, we perform a steady one-dimensional Eulerian-Eulerian simulation in the canonical configuration of a wall-stagnating spray flame. This configuration has recently been studied in detail in the context of spray combustion [59]. This configuration demonstrates a situation in which both gas and spray phases result in modeling error. As in the three-dimensional simulations considered, the gaseous inflow conditions correspond to air at $T_0 = 394\,\mathrm{K}$ and a system pressure of $p_0 = 2.07\,\mathrm{atm}$. The spray inflow conditions correspond to liquid Cat-A2 fuel at a temperature $T_l = 322\,\mathrm{K}$ and diameter $d_0 = 56\,\mu\mathrm{m}$. In the one-dimensional simulation, gaseous and liquid phases are injected with an axial velocity $u_0 = 0.17\,\mathrm{m/s}$ a distance $L = 10.0\,\mathrm{mm}$ from an isothermal wall at temperature $T_w = 1200\,\mathrm{K}$. The injected droplet number density is selected to give a global equivalence ratio of $\phi_0 = 1.94$. These values were chosen to achieve flame stabilization in the detached/freely-propagating regime, discussed in Ref. [59], to ensure the spray-flame interaction occurs away from the boundaries. The simulations are performed using FRC and the same chemical mechanism as the three-dimensional simulations, and the modeling error is computed in the same manner and using the same FPV table as the three-dimensional simulations.

One-dimensional simulation results are shown in Fig. A.1. The flow is from left to right, where the air and fuel spray are injected at $x/L = 1.0$ and the wall is at $x = 0.0$. In Fig. A.1(a), we find that significant spray evaporation begins around $x/L = 0.7$, as seen from the increase in the total evaporation rate $\dot{S}_\rho = n_l \dot{m}_d$ and consequently in the gaseous mixture fraction Z, where n_l is the local droplet number density. The flame is stabilized around $x/L = 0.6$, as seen from the temperature and Y_{OH} profiles. From the evaporation rate profile, it is evident that there is direct spray-flame in-

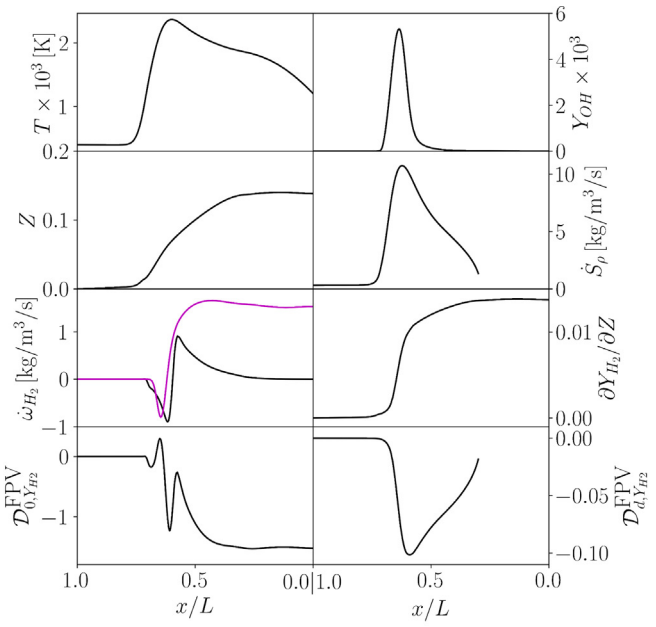

(a) In the $\dot{\omega}_{H_2}$ panel, the black and magenta lines indicates the source terms computed from FRC and FPV, respectively.

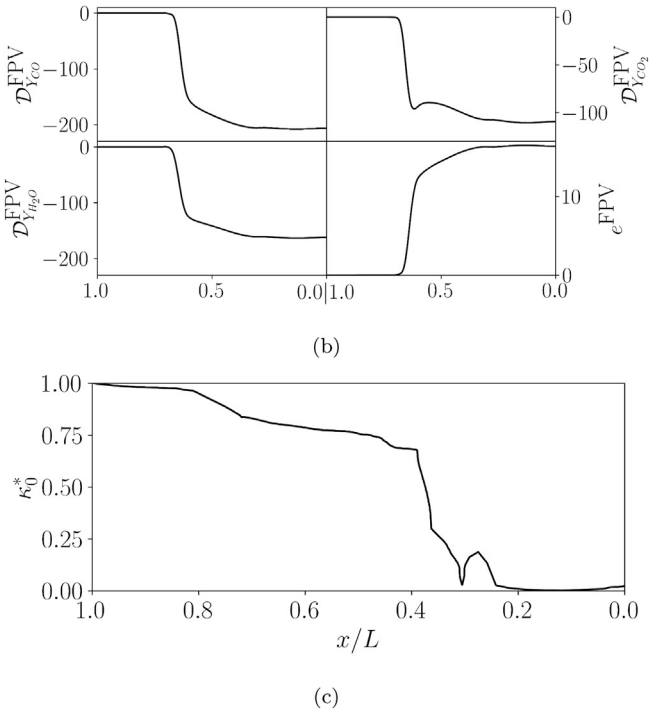

Fig. A.1. Steady one-dimensional wall-stagnating spray flame simulation results.

teraction in this case, with the spray penetrating the flame and continuing to evaporate to around $x/L = 0.3$. In the post-flame region, the product gases are cooled by heat losses to the evaporating spray as well as to the stagnation wall.

The derivations of Section 3 showed that the gaseous drift $\mathcal{D}^{\mathrm{FPV}}_{\psi,0}$ is due primarily to the difference in chemical source terms computed using the sub-models considered, and the drift arising from the spray $\mathcal{D}^{\mathrm{FPV}}_{\psi,d}$ is the negative of the product of the chemical sensitivity $\frac{\partial \psi_*^{\mathrm{FPV}}}{\partial Z}$ with the local evaporation source term $\dot{S}_\rho$. In Fig. A.1(a), we find that the chemical source terms are in close agreement for FPV and FRC prior to the flame, begin to diverge in the flame zone and remain substantially different in the exhaust gases, resulting in the $\mathcal{D}^{\mathrm{FPV}}_{\psi,0}$ profile shown. This is because FPV is able to adequately recover the chemical source term in the nearly adiabatic and low-reactivity region prior to the flame, but is less accurate in capturing the reactivity profile through the flame. Substantial heat losses to the isothermal wall and to spray evaporation quench the chemistry, an effect FPV is incapable of capturing. The H_2 source term is shown in the figure due to its strong sensitivity. The other species of the progress variable are qualitatively similar in their behavior, and are shown in Fig. A.1(b). FPV incurs a large modeling error in the exhaust region due to the sub-model's assumption of an adiabatic flow, as seen from the e^{FPV} profile in Fig. A.1(a). Considering the profile for $\frac{\partial \psi_*^{\mathrm{FPV}}}{\partial Z}$, we find that chemical sensitivity increases rapidly in the flame and remains high in the product gases. In the context of the profile for $\dot{S}_\rho$ in Fig. A.1(a), this results in the $\mathcal{D}^{\mathrm{FPV}}_{\psi,d}$ profile shown, which has the greatest magnitude in the flame zone where both the evaporation rate and chemical sensitivity are large. In the one-dimensional simulation considered here, $|\mathcal{D}^{\mathrm{FPV}}_{\psi,d}| \ll |\mathcal{D}^{\mathrm{FPV}}_{\psi,0}|$, but this is a result of the particularities of the boundary conditions chosen here. The stochastic nature of the three-dimensional turbulent simulations considered in the main body of this work results in a range of relative magnitudes for both drift term components, and is discussed in Section 5.2.

For the present one-dimensional steady case, the sub-model assignment behavior is readily evaluated. Figure A.1(a) shows the profile of κ_0^* throughout the domain, where $\kappa_0^*(x)$ is the lowest value of κ_0 for which FRC is assigned by the MCKP algorithm at each point x. For a given simulation undertaken with a user-specified cost parameter value κ_0, all domain locations where $\kappa_0 > \kappa_0^*$ in Fig. A.1(a) will be assigned to FRC. From the figure, we find that even in this one-dimensional case, the assignment behavior is spatially non-monotonic. Increasing κ_0 results in a greater portion of the domain being assigned to FRC, with the highly non-adiabatic near-wall region where $x/L < 0.2$ being assigned to FRC for all values of $\kappa_0 > 0.0$, and the near-inert region near the injector where $x/L > 0.8$ being assigned to FRC only when $\kappa_0 \to 1.0$; for the present choice of boundary conditions much of the reaction zone is assigned to FRC for $\kappa_0 > 0.7$. We find therefore that the behavior observed in this one-dimensional case is in alignment with the model assignment analyses we presented in Sections 3.3 and 5.1.

References

[1] H. Wang, R. Xu, K. Wang, C.T. Bowman, R.K. Hanson, D.F. Davidson, K. Brezinsky, F.N. Egolfopoulos, A physics-based approach to modeling real-fuel combustion chemistry—I. Evidence from experiments, and thermodynamic, chemical kinetic and statistical considerations, Combust. Flame 193 (2018) 502–519.

[2] L. Esclapez, P.C. Ma, E. Mayhew, R. Xu, S. Stouffer, T. Lee, H. Wang, M. Ihme, Fuel effects on lean blow-out in a realistic gas turbine combustor, Combust. Flame 181 (2017) 82–99.

[3] D. Mohaddes, W. Xie, M. Ihme, Analysis of low-temperature chemistry in a turbulent swirling spray flame near lean blow-out, Proc. Combust. Inst. 38 (2021) 3435–3443.

[4] A. Vié, B. Franzelli, Y. Gao, T. Lu, H. Wang, M. Ihme, Analysis of segregation and bifurcation in turbulent spray flames: a 3D counterflow configuration, Proc. Combust. Inst. 35 (2) (2015) 1675–1683, doi:10.1016/J.PROCI.2014.06.083.

[5] P.C. Ma, H. Wu, T. Jaravel, L. Bravo, M. Ihme, Large-eddy simulations of transcritical injection and auto-ignition using diffuse-interface method and finite-rate chemistry, Proc. Combust. Inst. 37 (3) (2019) 3303–3310, doi:10.1016/j.proci.2018.05.063.

[6] M. Ihme, W.T. Chung, A. Mishra, Combustion machine learning: principles, progress, and prospects, Prog. Energy Combust. Sci. 91 (2022) 101010.

[7] E. Fedina, C. Fureby, G. Bulat, W. Meier, Assessment of finite rate chemistry large eddy simulation combustion models, Flow Turbul. Combust. 99 (2) (2017) 385–409, doi:10.1007/s10494-017-9823-0.

[8] J.P. Légier, T. Poinsot, B. Varoquié, F. Lacas, D. Veynante, Large eddy simulation of a non-premixed turbulent burner using a dynamically thickened flame model, IUTAM Symposium on Turbulent Mixing and Combustion (2002), pp. 315–326.
[9] C.D. Pierce, P. Moin, Progress-variable approach for large-eddy simulation of non-premixed turbulent combustion, J. Fluid Mech. 504 (3) (2004) 73–97.
[10] M. Ihme, C.M. Cha, H. Pitsch, Prediction of local extinction and re-ignition effects in non-premixed turbulent combustion using a flamelet/progress variable approach, Proc. Combust. Inst. 30 (1) (2005) 793–800.
[11] M. Ihme, H. Pitsch, Modeling of radiation and nitric oxide formation in turbulent nonpremixed flames using a flamelet/progress variable formulation, Phys. Fluids 20 (5) (2008) 055110, doi:10.1063/1.2911047.
[12] F.L. Sacomano Filho, A. Hosseinzadeh, A. Sadiki, J. Janicka, On the interaction between turbulence and ethanol spray combustion using a dynamic wrinkling model coupled with tabulated chemistry, Combust. Flame 215 (2020) 203–220, doi:10.1016/j.combustflame.2020.01.038.
[13] H.H. Chiu, T.M. Liu, Group combustion of liquid droplets, Combust. Sci. Technol. 17 (3–4) (1977) 127–142, doi:10.1080/00102207708946823.
[14] F.L. Sacomano Filho, G. Kuenne, M. Chrigui, A. Sadiki, J. Janicka, A consistent artificially thickened flame approach for spray combustion using LES and the FGM chemistry reduction method: validation in lean partially pre-vaporized flames, Combust. Flame 184 (2017) 68–89, doi:10.1016/j.combustflame.2017.05.031.
[15] P.C. Ma, H. Wu, J.W. Labahn, T. Jaravel, M. Ihme, Analysis of transient blow-out dynamics in a swirl-stabilized combustor using large-eddy simulations, Proc. Combust. Inst. 37 (4) (2019) 5073–5082, doi:10.1016/J.PROCI.2018.06.066.
[16] Q. Wang, T. Jaravel, M. Ihme, Assessment of spray combustion models in large-eddy simulations of a polydispersed acetone spray flame, Proc. Combust. Inst. 37 (3) (2019) 3335–3344, doi:10.1016/j.proci.2018.06.011.
[17] C. Hollmann, E. Gutheil, Flamelet-modeling of turbulent spray diffusion flames based on a laminar spray flame library, Combust. Sci. Technol. 135 (1–6) (1998) 175–192, doi:10.1080/00102209808924156.
[18] D.C. Haworth, Progress in probability density function methods for turbulent reacting flows, Prog. Energy Combust. Sci. 36 (2) (2010) 168–259, doi:10.1016/j.pecs.2009.09.003.
[19] H.W. Ge, E. Gutheil, Simulation of a turbulent spray flame using coupled PDF gas phase and spray flamelet modeling, Combust. Flame 153 (1–2) (2008) 173–185, doi:10.1016/j.combustflame.2007.10.019.
[20] Y. Hu, H. Olguin, E. Gutheil, A spray flamelet/progress variable approach combined with a transported joint PDF model for turbulent spray flames, Combust. Theory Model. 21 (3) (2017) 575–602, doi:10.1080/13647830.2016.1277589.
[21] H. Wu, Y.C. See, Q. Wang, M. Ihme, A Pareto-efficient combustion framework with submodel assignment for predicting complex flame configurations, Combust. Flame 162 (11) (2015) 4208–4230.
[22] H. Wu, P.C. Ma, T. Jaravel, M. Ihme, Pareto-efficient combustion modeling for improved CO-emission prediction in LES of a piloted turbulent dimethyl ether jet flame, Proc. Combust. Inst. 37 (2) (2019) 2267–2276.
[23] Q. Douasbin, M. Ihme, C. Arndt, Pareto-efficient combustion framework for predicting transient ignition dynamics in turbulent flames: application to a pulsed jet-in-hot-coflow flame, Combust. Flame 223 (2021) 153–165.
[24] Q. Douasbin, M. Ihme, An NP-hard problem solver for the Pareto-efficient combustion framework, CTR Annu. Res. Briefs (2020) 253–263.
[25] M. Colket, J. Heyne, Fuel Effects on Operability of Aircraft Gas Turbine Combustors, Prog. Astronaut. Aero. AIAA, 2021.
[26] A. Panchal, R. Ranjan, S. Menon, Effect of chemistry modeling on flame stabilization of a swirl spray combustor, AIAA Paper 2018-4684 (2018).
[27] V.R. Hasti, P. Kundu, G. Kumar, S.A. Drennan, S. Som, S.H. Won, F.L. Dryer, J.P. Gore, Lean blow-out (LBO) computations in a gas turbine combustor, AIAA Paper 2018-4958 (2018).
[28] T. Poinsot, D. Veynante, Theoretical and Numerical Combustion, second ed., R.T, Edwards, 2005.
[29] R. Miller, K. Harstad, J. Bellan, Evaluation of equilibrium and non-equilibrium evaporation models for many-droplet gas-liquid flow simulations, Int. J. Multiph. Flow 24 (6) (1998) 1025–1055.
[30] W. Ranz, W. Marshall, Evaporation from drops, part I, Chem. Eng. Prog. 48 (3) (1952) 141–146.
[31] S.V. Apte, M. Gorokhovski, P. Moin, LES of atomizing spray with stochastic modeling of secondary breakup, Int. J. Multiph. Flow 29 (9) (2003) 1503–1522, doi:10.1016/S0301-9322(03)00111-3.
[32] M. Boivin, O. Simonin, K.D. Squires, On the prediction of gas-solid flows with two-way coupling using large eddy simulation, Phys. Fluids 12 (8) (2000) 2080–2090.
[33] E.J. Ching, M. Ihme, Efficient projection kernels for discontinuous Galerkin simulations of disperse multiphase flows on arbitrary curved elements, J. Comput. Phys. 435 (2021) 110266.
[34] S.B. Pope, Small scales, many species and the manifold challenges of turbulent combustion, Proc. Combust. Inst. 34 (1) (2013) 1–31, doi:10.1016/j.proci.2012.09.009.
[35] H. Wu, M. Ihme, Compliance of combustion models for turbulent reacting flow simulations, Fuel 186 (2016) 853–863.
[36] M. Ihme, L. Shunn, J. Zhang, Regularization of reaction progress variable for application to flamelet-based combustion models, J. Comput. Phys. 231 (23) (2012) 7715–7721, doi:10.1016/j.jcp.2012.06.029.
[37] P. Moin, S.V. Apte, Large-eddy simulation of realistic gas turbine combustors, AIAA J. 44 (4) (2006) 698–708.
[38] R. Xu, K. Wang, S. Banerjee, J. Shao, T. Parise, Y. Zhu, S. Wang, A. Movaghar, D.J. Lee, R. Zhao, X. Han, Y. Gao, T. Lu, K. Brezinsky, F.N. Egolfopoulos, D.F. Davidson, R.K. Hanson, C.T. Bowman, H. Wang, A physics-based approach to modeling real-fuel combustion chemistry II. Reaction kinetic models of jet and rocket fuels, Combust. Flame 193 (2018) 520–537.
[39] D. Pisinger, A minimal algorithm for the multiple-choice knapsack problem, Eur. J. Oper. Res. 83 (2) (1995) 394–410, doi:10.1016/0377-2217(95)00015-I.
[40] S. Stouffer, T. Hendershott, J. Monfort, J. Diemer, E. Corporan, P. Wrzesinski, A. Caswell, Lean blowout and ignition characteristics of conventional and surrogate fuels measured in a swirl stabilized combustor, AIAA Paper 2017-1954 (January) (2017).
[41] J.R. Monfort, S.D. Stouffer, T.H. Hendershott, P.J. Wrzesinski, W.S. Foley, K.D. Rein, Evaluating combustion instability in a swirl-stabilized combustor using simultaneous pressure, temperature, and chemiluminescence measurements at high repetition rates, AIAA Paper 2017-1101 (January) (2017).
[42] J.G. Colborn, J.S. Heyne, S.D. Stouffer, T.H. Hendershott, E. Corporan, Chemical and physical effects on lean blowout in a swirl-stabilized single-cup combustor, Proc. Combust. Inst. 38 (4) (2021) 6309–6316, doi:10.1016/j.proci.2020.06.119.
[43] M. Colket, J. Heyne, M. Rumizen, M. Gupta, T. Edwards, W.M. Roquemore, G. Andac, R. Boehm, J. Lovett, R. Williams, J. Condevaux, D. Turner, N. Rizk, J. Tishkoff, C. Li, J. Moder, D. Friend, V. Sankaran, Overview of the national jet fuels combustion program, AIAA J. 55 (4) (2017) 1087–1104.
[44] C. Shao, K. Maeda, M. Ihme, Analysis of core-noise contributions in a realistic gas-turbine combustor operated near lean blow-out, Proc. Combust. Inst. 38 (4) (2021) 6203–6211.
[45] C. Shao, D. Brouzet, N. Rock, M. Ihme, Parametric analysis of core-noise from a realistic gas-turbine combustor for cruise and take-off conditions, Appl. Energy Combust. Sci. 9 (2022) 100045, doi:10.1016/j.jaecs.2021.100045.
[46] H. Wang, X. You, A.V. Joshi, S.G. Davis, A. Laskin, F. Egolfopoulos, C.K. Law, USC Mech Version II: High-Temperature Combustion Reaction Model of H2/CO/C1–C4 Compounds, 2007, (http://www.ignis.usc.edu/USC_Mech_II.htm).
[47] Y. Khalighi, J.W. Nichols, S.K. Lele, F. Ham, P. Moin, Unstructured large eddy simulation for prediction of noise issued from turbulent jets in various configurations, AIAA Paper 2011-2886 (2011).
[48] P.C. Ma, Y. Lv, M. Ihme, An entropy-stable hybrid scheme for simulations of transcritical real-fluid flows, J. Comput. Phys. 340 (2017) 330–357.
[49] H. Wu, P.C. Ma, M. Ihme, Efficient time-stepping techniques for simulating turbulent reactive flows with stiff chemistry, Comput. Phys. Commun. 243 (2019) 81–96.
[50] V.R. Hasti, P. Kundu, G. Kumar, S.A. Drennan, S. Som, J.P. Gore, Numerical simulation of flow distribution in a realistic gas turbine combustor, AIAA Paper 2018-4956 (2018). 10.2514/6.2018-4956
[51] A.W. Vreman, An eddy-viscosity subgrid-scale model for turbulent shear flow: algebraic theory and applications, Phys. Fluids 16 (10) (2004) 3670–3681.
[52] F. Charlette, C. Meneveau, D. Veynante, A power-law flame wrinkling model for LES of premixed turbulent combustion part II: dynamic formulation, Combust. Flame 131 (1–2) (2002) 181–197, doi:10.1016/S0010-2180(02)00401-7.
[53] W.T. Chung, A.A. Mishra, N. Perakis, M. Ihme, Data-assisted combustion simulations with dynamic submodel assignment using random forests, Combust. Flame 227 (2021) 172–185, doi:10.1016/j.combustflame.2020.12.041.
[54] N. Rock, S. Stouffer, T. Hendershott, E. Corporan, P. Wrzesinski, Characterization of coherent flow structures in a swirl-stabilized spray combustor, AIAA Paper 2021-0791 (2021). 10.2514/6.2021-0791
[55] L. Ma, D. Roekaerts, Numerical study of the multi-flame structure in spray combustion, Proc. Combust. Inst. 36 (2017) 2603–2613, doi:10.1016/j.proci.2016.06.015.
[56] A. Ateshkadi, V.G. McDonell, G.S. Samuelsen, Lean blowout model for a spray-fired swirl-stabilized combustor, Proc. Combust. Inst. 28 (2000) 1281–1288, doi:10.1016/S0082-0784(00)80341-0.
[57] A. Verdier, J. Marrero Santiago, A. Vandel, G. Godard, G. Cabot, B. Renou, Local extinction mechanisms analysis of spray jet flame using high speed diagnostics, Combust. Flame 193 (2018) 440–452, doi:10.1016/j.combustflame.2018.03.032.
[58] A.J. Bokhart, D. Shin, R. Gejji, T. Buschhagen, S.V. Naik, R.P. Lucht, J.P. Gore, P. Sojka, S.E. Meyer, Spray measurements at elevated pressures and temperatures using phase Doppler anemometry, AIAA Paper 2017-0828 (2017).
[59] D. Mohaddes, M. Ihme, Wall heat transfer and flame structure transitions in stagnating spray flames, Proc. Combust. Inst. 39 (2023) In press, doi:10.1016/j.proci.2022.08.037.